

SPECTROSCOPIC PROPERTIES OF COOL STARS (SPOCS). I. 1040 F, G, AND K DWARFS FROM KECK, LICK, AND AAT PLANET SEARCH PROGRAMS

JEFF A. VALENTI

Space Telescope Science Institute, 3700 San Martin Drive, Baltimore, MD 21218; valenti@stsci.edu

AND

DEBRA A. FISCHER

Department of Physics and Astronomy, San Francisco State University, San Francisco, CA 94132; fischer@stars.sfsu.edu

Received 2004 September 25; accepted 2005 March 21

ABSTRACT

We present a uniform catalog of stellar properties for 1040 nearby F, G, and K stars that have been observed by the Keck, Lick, and AAT planet search programs. Fitting observed echelle spectra with synthetic spectra yielded effective temperature, surface gravity, metallicity, projected rotational velocity, and abundances of the elements Na, Si, Ti, Fe, and Ni, for every star in the catalog. Combining *V*-band photometry and *Hipparcos* parallaxes with a bolometric correction based on the spectroscopic results yielded stellar luminosity, radius, and mass. Interpolating Yonsei-Yale isochrones to the luminosity, effective temperature, metallicity, and α -element enhancement of each star yielded a theoretical mass, radius, gravity, and age range for most stars in the catalog. Automated tools provide uniform results and make analysis of such a large sample practical. Our analysis method differs from traditional abundance analyses in that we fit the observed spectrum directly, rather than trying to match equivalent widths, and we determine effective temperature and surface gravity from the spectrum itself, rather than adopting values based on measured photometry or parallax. As part of our analysis, we determined a new relationship between macroturbulence and effective temperature on the main sequence. Detailed error analysis revealed small systematic offsets with respect to the Sun and spurious abundance trends as a function of effective temperature that would be inobvious in smaller samples. We attempted to remove these errors by applying empirical corrections, achieving a precision per spectrum of 44 K in effective temperature, 0.03 dex in metallicity, 0.06 dex in the logarithm of gravity, and 0.5 km s⁻¹ in projected rotational velocity. Comparisons with previous studies show only small discrepancies. Our spectroscopically determined masses have a median fractional precision of 15%, but they are systematically 10% higher than masses obtained by interpolating isochrones. Our spectroscopic radii have a median fractional precision of 3%. Our ages from isochrones have a precision that varies dramatically with location in the Hertzsprung-Russell diagram. We plan to extend the catalog by applying our automated analysis technique to other large stellar samples.

Subject headings: catalogs — stars: abundances — stars: fundamental parameters — stars: late-type — techniques: spectroscopic

Online material: color figures, machine-readable tables

1. INTRODUCTION

Using radiative transfer and model stellar atmospheres to analyze high-resolution spectra yields fundamental measurements of stellar temperature, gravity, rotation, and composition. These primary results are used to calibrate secondary diagnostics, which are then used to test models of stellar structure, stellar atmospheres, angular momentum evolution, and Galactic chemical evolution. In principle, the results of high-resolution analyses can be used to test directly these models, but until recently data have been sparse and the labor required to analyze high-resolution spectra has generally precluded large samples.

Over the past decade, radial velocity searches for extrasolar planets (e.g., Cummings et al. 1999; Butler et al. 2003) and other large spectroscopic surveys have yielded high-resolution echelle spectra of thousands of cool stars (e.g., Moularka et al. 2004). At the same time, computer hardware and astronomical software have evolved significantly, making the analysis of large samples practical. Motivated by these two advances, we analyzed echelle spectra of more than a thousand cool stars, as described below.

In a companion paper, we investigate the correlation between stellar metallicity, [M/H], and the occurrence of giant planets (Fischer & Valenti 2005). We use the stellar properties determined

here to account for selection biases in the planet search sample (see § 2.1). These biases must be considered carefully before using the catalog for other purposes, such as studies of Galactic chemical evolution. In the future, we plan to analyze existing echelle spectra of thousands of additional stars. This uniform catalog of stellar properties will support a broad range of astrophysical applications and help refine spectroscopic analysis techniques.

There is currently no standard method for analyzing high-resolution spectra, so different studies (even by the same investigator) often yield significantly different results for the same star. These differences are due to choice of atomic data, model atmosphere, analysis technique, numerical method, etc. Compilations like Cayrel de Strobel et al. (2001) reveal a scatter in results caused by systematic errors in current methods. Random errors within a study are often smaller than systematic errors, so uniform analysis of a large stellar sample can yield the precision and statistical significance needed to address various problems.

Traditional abundance analysis begins with adoption of an effective temperature (T_{eff}) and surface gravity ($\log g$), based on photometry and perhaps parallax. Radiative transfer is then used to solve for the elemental abundance required to reproduce the observed equivalent width of each isolated spectral line. Microturbulence (v_{mic}) is adjusted to remove any trend in abundance

for individual transitions as a function of lower excitation potential. McWilliam (1990), Balachandran (1990), and Edvardsson et al. (1993) are classic examples of this approach.

Our analysis method differs from the traditional method in that we fit the observed spectrum directly, rather than trying to match equivalent widths. Allende Prieto et al. (2004) is a recent example of a study that fitted line profiles. However, we go further and determine T_{eff} and $\log g$ from the spectrum itself, rather than adopting values a priori based on measured photometry or parallax. We then use a subset of our spectroscopically determined stellar properties (T_{eff} , $\log g$, $[M/H]$, and α -element enhancement) to obtain an accurate bolometric correction and appropriate evolutionary models for each star. For stars with photometry and parallax measurements, the evolutionary models provide a second estimate of $\log g$ and additional stellar properties (mass, age constraints).

Interpreting photometry after a purely spectroscopic analysis may not yield the most accurate results when an excellent parallax is also available, but this approach allows us to model all spectra uniformly, regardless of whether auxiliary constraints are available. Segregating spectroscopic and photometric constraints also decouples the influence of stellar atmospheric and evolutionary models, allowing self-consistency tests and independent calibration of secondary diagnostics. Ultimately, all available constraints should be reconciled in the context of a fully self-consistent analysis. Studies such as this are a useful step toward that goal.

As sample sizes reach hundreds or thousands of stars, data reduction and analysis procedures must be highly automated to be practical. Automated data reduction pipelines are common now (e.g., Nichols & Linsky 1996; Mulas et al. 2002; Piskunov & Valenti 2002), but automated abundance analysis tools (e.g., McWilliam 1990; Valenti & Piskunov 1996; Erspamer & North 2002) are still rare. As sample sizes increase, the labor required to implement and test automated analysis pipelines will eventually be less than the labor required to analyze each spectrum manually. Automated analysis tools also yield more uniform results and make it practical to repeat and extend the analysis as algorithms evolve. In this study, we adopt and extend the automated analysis package described by Valenti & Piskunov (1996).

In the remainder of this paper we present a uniform spectroscopic analysis of 1944 spectra for a sample of 1040 FGK stars in planet search programs at Keck Observatory, Lick Observatory, and the Anglo-Australian Telescope (AAT). As outlined above, we first determine stellar parameters by fitting the observed spectrum and then use the results to analyze auxiliary measurements. By analyzing such a large sample with redundant observations, we are able to accurately assess random errors, which can exceed formally derived uncertainties. Our adopted uncertainties are 44 K for T_{eff} , 0.06 dex for $\log g$, 0.03 dex for $[Fe/H]$, and 0.5 km s^{-1} for $v \sin i$.

This paper is organized as follows. After this introduction (§ 1), we briefly describe the stellar sample, observations, data reduction, instrumental profile, wavelength calibration, and continuum normalization (§ 2). We then describe available atomic and molecular line data and corrections that we determined by fitting the solar spectrum (§ 3). We describe the model atmospheres, abundances, microturbulence, line broadening kernels, and the new macroturbulence relationship that we determined (§ 4). We describe the free parameters, methodology, and computer resources that we used to fit observed spectra (§ 5). We describe in detail corrections that we applied to our raw results to reproduce solar properties, yield consistent abundances in bi-

TABLE 1
SAMPLE CHARACTERISTICS

Parameter	Min.	Med.	Max.
T_{eff} (K).....	4707	5755	6594
$\log g$ (cgs).....	3.1	4.4	5.1
$[M/H]$	-1.9	0.0	0.5
$v \sin i$ (km s $^{-1}$).....	0.0	2.4	54.7
v_{rad} (km s $^{-1}$).....	-245	1	310
d (pc).....	1.3	33.2	202.4
V (mag).....	0.0	7.1	10.8
M_{bol} (mag).....	0.2	4.4	10.6

naries, and remove trends in abundance ratios with temperature (§ 6). In the same section, we also compare results for different initial parameter values and for multiple observations of the same star to assess the precision of our final results (§ 6). We then present our main tables of spectroscopically determined stellar parameters and derived auxiliary quantities (§ 7), comparing with theoretical isochrones, well measured gravities and radii, and previous analyses in the literature (§ 8). Finally, we summarize our main conclusions (§ 9), leaving many possible applications of our results to future studies.

The main body of this paper documents details of our procedure that will likely be important only to specialists engaged in similar analyses. We advise those interested only in our results to begin with the brief description of the stellar sample (§ 2.1) and then skip directly to the results (§§ 7.1, 7.2), returning to the discussion of precision (Table 6) for quantitative applications. The main catalog is available in machine-readable form from the Journal or the authors, and it is available in a relational database maintained by the VizieR service.

2. SPECTRAL DATA

2.1. Sample Description

We performed a serendipitous analysis of stars observed at least once by the Keck, Lick, and AAT planet search programs (Cummings et al. 1999; Fischer et al. 1999; Butler et al. 2003; Marcy et al. 2004, 2005), so our sample is defined by the selection criteria of these programs. These planet search programs monitor stars of spectral class F, G, K, and M, which have spectral lines sharp enough to yield precise radial velocities. These programs typically do not monitor stars that are chromospherically very active or in binaries with separations less than $2''$, but occasionally they do obtain one or more spectra of such objects.

We analyzed all F, G, and K stars observed from 1996 to 2003 by the Keck, Lick, and AAT planet search programs, regardless of whether the stars have been monitored for planets. Our initial sample consisted of 1140 stars. After discarding 19 double-lined spectroscopic binaries and 81 stars with effective temperatures (T_{eff}) cooler than 4700 K, we were left with 1040 stars in our final sample.

Table 1 gives characteristics for stars in our sample, listing minimum, median, and maximum values of effective temperature (T_{eff}), logarithmic surface gravity ($\log g$), metallicity ($[M/H]$), maximum projected rotational velocity ($v \sin i$), radial velocity relative to the solar system barycenter (v_{rad}), distance from Earth (d), apparent Johnson visual magnitude (V), and bolometric magnitude (M_{bol}). These characteristics come from the literature or from our spectroscopic analysis, as described in the remainder of this paper.

TABLE 2
SPECTROGRAPH FORMATS

Observatory	λ (Å)	m	$m\lambda$ (Å)
Keck	3889–6188	58–91	353874–358952
AAT	4825–8665	66–117	564185–572329
Lick	4728–9583	60–120	567308–575045

2.2. Observations

We made serendipitous use of high-quality “template” spectra obtained as part of the Keck, Lick, and AAT planet search programs (e.g., Cummings et al. 1999; Butler et al. 2003). Most planet search observations are obtained with an I_2 absorption cell in the light path to imprint a wavelength fiducial on each spectrum, but at least one template observation of each star is obtained without the I_2 cell. In this study, we model these low-noise ($\sim 0.3\%$ of the continuum) template spectra, obtained without the I_2 absorption cell. Before and after each template observation, one or more hot stars are observed with the iodine cell, providing a contemporaneous measurement of the instrumental profile.

Spectra were obtained with the High-Resolution Echelle Spectrometer (HIRES) on the 10 m telescope at Keck Observatory (Vogt et al. 1994), the University College London Echelle Spectrograph (UCLES) on the 4 m Anglo-Australian Telescope (AAT) at Siding Spring Observatory (Diego et al. 1990), and the Hamilton echelle spectrometer at Lick Observatory (Vogt 1987). Observations at Lick were obtained with both the 3 m Shane telescope and the 0.6 m coude auxiliary telescope (CAT). All three of these spectrographs yielded a typical resolving power (R) of about 70,000, except for a few observations obtained with an atypical slit width.

Table 2 gives the typical spectrograph formats used by the planet search projects at each observatory. After allowing some margin for stellar radial velocity shifts, the intersection of these three spectrograph formats is the wavelength interval 4830–6180 Å.

We initially analyzed 1944 spectra of 1140 stars but then excluded 25 spectra of 19 double-lined spectroscopic binaries and 112 spectra of 81 stars with T_{eff} below 4700 K, where our analysis becomes less robust due to significant blending by spectral lines with poorly known atomic and molecular line data. The remaining 1807 spectra of 1040 stars came from Keck, AAT, and Lick with the distribution 750, 793, and 264.

The planet search teams kindly provided us with extracted spectra from their standard data reduction pipeline, which is derived from the automated echelle reduction package of Valenti (1994), but with improved cosmic ray rejection, global background subtraction, and local sky subtraction. We converted the summed analog-to-digital units (ADUs) in each extracted pixel to summed electrons, using the gain appropriate for each detector. We then assigned uncertainties to each extracted pixel, assuming the only significant noise sources were detector read noise and Poisson fluctuations in the detection rate of stellar photons.

2.3. Instrumental Profile

When fitting spectra directly, accurate knowledge of the instrumental profile is needed to infer astrophysical line broadening. The planet search teams measure the instrumental profile at the time of each observation made with an I_2 cell (Valenti et al. 1995; Butler et al. 1996). Observations of hot stars with the I_2 cell yield instrumental profiles before and after each block of template observations, which are obtained without an I_2 cell. We

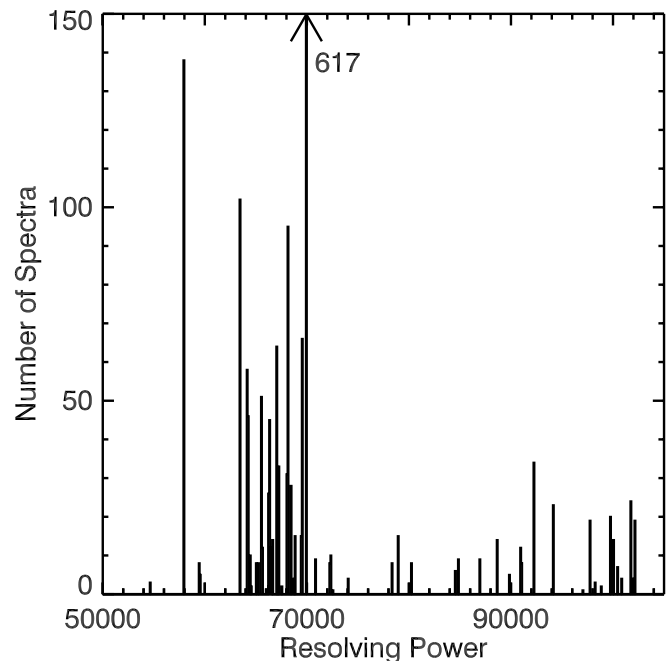


FIG. 1.—Distribution of resolutions for Keck, AAT, and Lick spectra. The effect of different slit widths must be modeled properly to accurately quantify astrophysical line broadening due to macroturbulence and rotation. [See the electronic edition of the *Journal* for a color version of this figure.]

fitted each reconstructed instrumental profile with a Gaussian function, thereby measuring effective resolution with 2% precision. We compared our I_2 resolutions to the median width of thorium emission lines in spectra of a hollow-cathode lamp, finding that generally the two methods yield consistent results when the slit is narrow.

For Keck spectra we adopted a single mean resolution for each slit width, ignoring changes in measured resolution as large as 5% from night to night. For AAT and Lick spectra, we adopted a different mean resolution for each night, tracking changes in measured resolution as large as 5%. Either approach is reasonable, given the precision of our measurements of resolution. A 2% error in measured resolution corresponds roughly to a 0.4 km s^{-1} error in $v \sin i$ at $v \sin i = 1 \text{ km s}^{-1}$, dropping to 0.1 km s^{-1} at $v \sin i = 5 \text{ km s}^{-1}$. Figure 1 shows the distribution of adopted resolutions for our set of template spectra.

2.4. Wavelength Calibration

For observations obtained with an I_2 cell, the planet search teams determined the instantaneous observatory frame wavelength scale from 5000 to 5900 Å by comparing I_2 lines imprinted on the stellar spectrum with a laboratory FTS spectrum of the I_2 cell. Nidever et al. (2002) used these I_2 wavelength solutions to determine radial velocities for many stars in our sample, achieving an accuracy of better than 0.1 km s^{-1} , after applying a zero-point offset of 0.52 km s^{-1} .

We find that the I_2 wavelength solutions usually drift systematically over the course of a night, with a typical amplitude of 1 km s^{-1} . Contemporaneous spectra of a hollow cathode thorium-argon lamp show identical trends. The observed drift is consistent with expected changes in the index of refraction of air, as the spectrograph cools by a couple of kelvin over the course of a night.

Our template spectra were obtained without an I_2 cell, so we cannot determine simultaneous I_2 wavelength scales. However, I_2 and thorium wavelength scales are often available for the beginning and end of each night. Because we are interested in

spectral intervals not covered by the I_2 wavelength scale, we adopted the thorium lamp as a wavelength reference.

For AAT, Lick, and many Keck spectra, we used the procedure described in Hinkle et al. (2000) to analyze each thorium calibration spectrum. We fitted a polynomial function of m and $m\lambda$ to measured positions of 1000–2000 thorium emission lines, obtaining rms residuals of 0.06, 0.15, and 0.10 km s⁻¹ for Keck, AAT, and Lick. We generally did not interpolate between wavelength scales for the beginning and end of each night, so nightly drift limits the typical accuracy of our observatory frame wavelength scales to roughly 1 km s⁻¹.

We transformed observatory wavelength scales to the rest frame of the solar system barycenter and then to the stellar rest frame. For the latter transformation, we used an initial estimate of the radial velocity, which we subsequently refined (see § 5). For a few Keck spectra, we empirically adjusted a generic wavelength scale by cross-correlating features in the observed spectrum with the corresponding features in the solar spectrum (Kurucz et al. 1984), yielding the wavelength scale in the stellar rest frame.

2.5. Continuum Normalization

Spectra from the planet search projects are generally not flux calibrated, so we divided each extracted spectrum by the apparent stellar continuum to remove instrumental sensitivity variations, yielding a residual intensity spectrum. We also applied an additional continuum normalization correction during the synthetic spectrum fitting procedure (see § 5.1).

To achieve self-consistent results for nearly 2000 spectra, we had to automate our continuum normalization procedure. The procedure is not simple, but visual inspection shows that the results are typically good to better than 1%, even for early K dwarfs. Conceptually, the algorithm first replaces relatively deep spectral features with higher values from neighboring echelle orders and then fits the high points in each order with a polynomial.

The algorithm operates on a two-dimensional array that initially contains all the extracted echelle orders for a given observation. A 3×3 pixel median filter replaces bad pixels and deep spectral features with values closer to the continuum. Then a scale factor is applied to each order to force 1% of the scaled data to exceed unity. To filter out additional spectral features, scaled pixels are then replaced by the mean of corresponding pixels in the two adjacent orders, if that substitution increases the value of a pixel.

The algorithm then identifies and fits the apparent continuum in each echelle order, starting with a linear function and ending after 5 iterations with a sixth-order polynomial. Continuum levels are determined in 5–20 bins across each order, such that in each bin a specified fraction of the pixel values exceeds the adopted continuum level. This fraction starts at 5% and ends in the final iteration at 30%, as line cores and the wings are progressively excluded from consideration successive iterations. In the final iteration, only residual intensities within 5% of unity are considered. We then divide each original extracted order by the polynomial continuum estimate and scale the final result so that 5% of the scaled data exceed unity.

Line blending becomes more severe in the blue and in cooler stars, making continuum placement and derived stellar parameters less accurate. For this reason, we ultimately decided to exclude from our analysis laboratory wavelengths shortward of 6000 Å, except for a spectral segment that includes the gravity-sensitive Mg I b triplet lines. Table 3 lists the wavelength segments we analyzed.

3. LINE DATA

Accurate spectrum synthesis analysis requires accurate opacities as a function of wavelength and position in the atmosphere.

TABLE 3
WAVELENGTH INTERVALS

λ_{beg}	λ_{end}	Lines	Keck	Lick	AAT
6000.....	6030	117	59	95	94/95
6030.....	6050	60	59	94/95	94
6050.....	6070	49	59	94	94
6100.....	6118	74	58	93/94	93
6121.....	6140	74	58	93	92/93
6143.....	6159	72	58	93	92
6160.....	6180	80	58	93	92

In the atmospheres of cool stars, millions of atomic and molecular lines have significant opacity. Unfortunately, existing line data from laboratory measurements and theoretical calculations are generally not accurate enough to reproduce our template spectra or indeed any observed spectrum with even moderate resolution and S/N ratio. This lack of accurate line data remains the single most daunting aspect of direct quantitative spectroscopic analysis, significantly impeding our ability to understand fundamental physical processes in the atmospheres of cool stars. To deal with this problem, we first gathered existing atomic and molecular line data and then used the solar spectrum to constrain empirical corrections.

3.1. Atomic Lines

In 2003 January, we obtained atomic line data from the Vienna Atomic Line Database (Piskunov et al. 1995; Kupka et al. 1999). The database is dominated by line data from Kurucz (1993b, 1994a, 1994b, 1994c), but more recent results are incorporated periodically. We used VALD “extract stellar” queries to obtain line data in our wavelength intervals for transitions with predicted absorption cores deeper than 0.5% of the continuum. For the VALD queries, we used solar abundances, v_{mic} of 0.7, $\log g$ of 4.5, and T_{eff} of 4000 and 5770 K. Line lists for the two effective temperatures were merged to produce a single line list with all the transitions expected to be significant in G- or K-type dwarfs. For F-type dwarfs, we may have missed a few weak lines that appear above 6000 K.

For lines without a van der Waals damping parameter (Γ_6) in VALD, we used the Unsöld approximation (Unsöld 1955) to obtain an initial estimate. We then multiplied all Γ_6 values by an ad hoc enhancement factor of 2.5 (e.g., Valenti & Piskunov 1996). This global enhancement factor often improves the Unsöld approximation, but it should not be applied to more accurate Γ_6 values (e.g., Barklem et al. 2000) that VALD returns for some lines. As described below, we used the solar spectrum to determine empirical corrections for initial values of Γ_6 that did not adequately reproduce observed line profiles.

3.2. Molecular Lines

On 2003 December 9, we obtained line data for various isotopes of the molecules C_2 , CN, and MgH from the Kurucz Web site.¹ The site attributed the line data to Kurucz (1993b).

Wavelengths of molecular lines can differ significantly for different isotopes, due to changes in molecular moment of inertia and hence rotational energy. However, SME does not distinguish between different isotopes of the same element because SME was originally designed for use with atomic lines, which generally have similar characteristics for all isotopes. To handle isotopes in

¹ <http://kurucz.harvard.edu/LINELISTS/LINESMOL/>.

SME, we multiplied the Kurucz oscillator strengths for molecular lines by our adopted isotopic fractions for the constituent elements. This procedure should be mathematically equivalent to apportioning elemental abundances to different isotopes.

We adopted the following isotopic fractions: 98.9% ^{12}C , 1.1% ^{13}C , 99.63% ^{14}N , 0.37% ^{15}N , 78.7% ^{24}Mg , 10.1% ^{25}Mg , and 11.2% ^{26}Mg . The C and N fractions come from Anders & Grevesse (1989), while the Mg fractions differ slightly from the preferred values in de Bièvre & Barnes (1985). Only Mg has more than one significant isotope.

The Kurucz data files contained 52,773 C_2 , 7122 CN, and 17,935 MgH lines in our wavelength intervals. A small fraction of these lines contribute significant opacity. We used the formalism of Valenti et al. (1998) to estimate the strength (S) of each line, assuming a characteristic excitation temperature of 4000 K in atmospheric layers where molecular lines form. For the spectrum synthesis analysis, we retained only 78 C_2 and zero CN lines with $S > 1.4$ and 247 MgH lines with $S > 2.1$. Restricting the number of lines was necessary to make the analysis of so many spectra computationally feasible.

3.3. Empirical Line Data Corrections

Starting with the atomic and molecular line data just described, we used SME to determine empirical line data corrections that improved agreement between synthetic and observed spectra of the Sun.

The observed solar spectrum (Wallace et al. 1998) was obtained with a $5''$ circular aperture at the center ($\mu = 1$) of a defocused solar image. For our wavelength intervals, the unapodized instrumental profile is a sinc function with a full width at half-maximum of 0.084 cm^{-1} , yielding a resolving power of 200,000. Wallace et al. (1998) identified and removed telluric absorption from the atlas spectrum. Our wavelength intervals contain only about 20 detectable telluric lines shortward of 6020 \AA with absorption cores no deeper than 4% at an air mass of 2.5. We ignore these few telluric absorption lines in our stellar spectra, which are obtained at lower air mass and lower spectral resolution.

When modeling the Sun to refine line data, we adopted the following atmospheric parameters: $T_{\text{eff}} = 5770 \text{ K}$, $\log g = 4.44$, $[\text{M}/\text{H}] = 0.0$, $v_{\text{mic}} = 0.866 \text{ km s}^{-1}$, $v_{\text{mac}} = 3.57 \text{ km s}^{-1}$, $v \sin i = 0.0 \text{ km s}^{-1}$ (disk center), $v_{\text{rad}} = 0.0 \text{ km s}^{-1}$. In subsequent stellar analyses, we adopted $v_{\text{mic}} = 0.85 \text{ km s}^{-1}$ and $v_{\text{mac}} = 3.54 \text{ km s}^{-1}$ at $T_{\text{eff}} = 5770 \text{ K}$. These minor inconsistencies are insignificant. Because the observed spectrum was obtained at disk center, we calculated the emergent intensity at $\mu = 1.0$, rather than the disk-integrated emergent flux.

We used SME to determine empirical line data corrections that yielded the best agreement between observed and synthetic spectra of the Sun. We adjusted line data only for lines with significant discrepancies. For lines with significant damping wings, we solved for both Γ_6 and $\log gf$. For weaker lines, we solved only for $\log gf$. We adjusted line data first for the strongest lines and then for progressively weaker blends. We also adjusted the central wavelengths of a few lines. Some wavelength intervals contain observed spectral lines with no analog in our line data. We defined a mask to ignore these wavelength intervals during the line data analysis and during subsequent stellar analyses.

4. SPECTRUM SYNTHESIS

We used version 2.1 of the software package Spectroscopy Made Easy (SME) to generate synthetic spectra and to fit observed spectra. We document here modifications to SME since version 1 (Valenti & Piskunov 1996) and give specific settings that were used for this project. The equation of state, opacity, and

radiative transfer in SME were written by N. Piskunov in C++ and compiled into a shared library. Changes to the equation of state routine have already been described by Valenti et al. (1998). SME now uses a Feautrier (rather than Runge-Kutta) technique to solve the radiative transfer equation, trading some precision (0.3%) for quicker execution. Modular routines written in the Interactive Data Language (IDL) combine the intensity profiles, fit an observed spectrum, and provide a graphical user interface.

4.1. Model Atmospheres

Calculating a self-consistent model of the temperature, density, and pressure throughout a stellar atmosphere is computationally expensive. Moreover, interpolating 8 atmospheres in a three-dimensional grid and then synthesizing 1 spectrum is more efficient than synthesizing spectra at 8 grid points and then interpolating the results. Given the size of our sample and the number of free parameters, efficiency dictated that we interpolate model atmospheres in a precomputed grid.

We adopted the Kurucz (1992) grid of model atmospheres generated by the ATLAS9 program (Kurucz 1993a). The cool star portion of the grid includes $T_{\text{eff}} = 3500\text{--}8000 \text{ K}$ in steps of 250 K, $\log g = 0.0$ to 5.0 in steps of 0.5 , and $[\text{M}/\text{H}] = -5.0$ to 1.0 in steps of 0.5 with finer steps of 0.1 for $[\text{M}/\text{H}] = -0.3$ to 0.3 . Kurucz (1992) calculated these atmospheres assuming a turbulent velocity of 2 km s^{-1} and mixing length to pressure scale height ratio of 1.25 .

Accurately interpolating two model atmospheres in a relatively coarse grid requires care because atmospheric quantities at a fixed mass column density (m) are not linear functions of T_{eff} , $\log g$, and $[\text{M}/\text{H}]$, even when all quantities are expressed logarithmically. In some cases, interpolation accuracy is improved significantly by adjusting the depth scales of the atmospheres being interpolated, aligning analogous features at different depths. An example of such a feature is the steep temperature gradient where hydrogen ionization fraction begins to increase rapidly with depth. The mass column density of this feature in the temperature structure depends on T_{eff} . Figure 2 shows that significant interpolation errors can occur, if changes in the depth of this feature are ignored. We have not investigated whether similar behavior occurs when using a depth scale based on optical depth, rather than mass column.

SME has a new routine (`interp_atmo_pair`) that interpolates atmospheres at two grid nodes, empirically compensating for shifts in the mass column density of atmospheric features. The interpolation function shifts and scales logarithmic temperature, density, or pressure as a function of shifted logarithmic mass column density. The routine first determines shift and scaling parameters needed to best map one atmosphere in the grid onto the other. Then a fraction of this full shift and scaling is applied to both grid atmospheres to transform them to the desired T_{eff} , $\log g$, and $[\text{M}/\text{H}]$. Finally, the routine averages the two transformed atmospheres at all depths in common, extrapolating as needed using only one transformed atmosphere. The middle panel of Figure 2 illustrates this procedure.

We tested the new routine by interpolating across two grid nodes and comparing the result with the intermediate node. For solar-type stars, the maximum fractional error in temperature dropped from 10% to 1% and the median absolute value of the error dropped from 2% to 0.2%, relative to the old algorithm. In normal operation, errors will be less than half this amount, since interpolation spans less than one step in the grid, rather than the two full steps used in the error analysis.

We used the solar elemental abundance pattern from Anders & Grevesse (1989) as a template for stellar abundances, except that

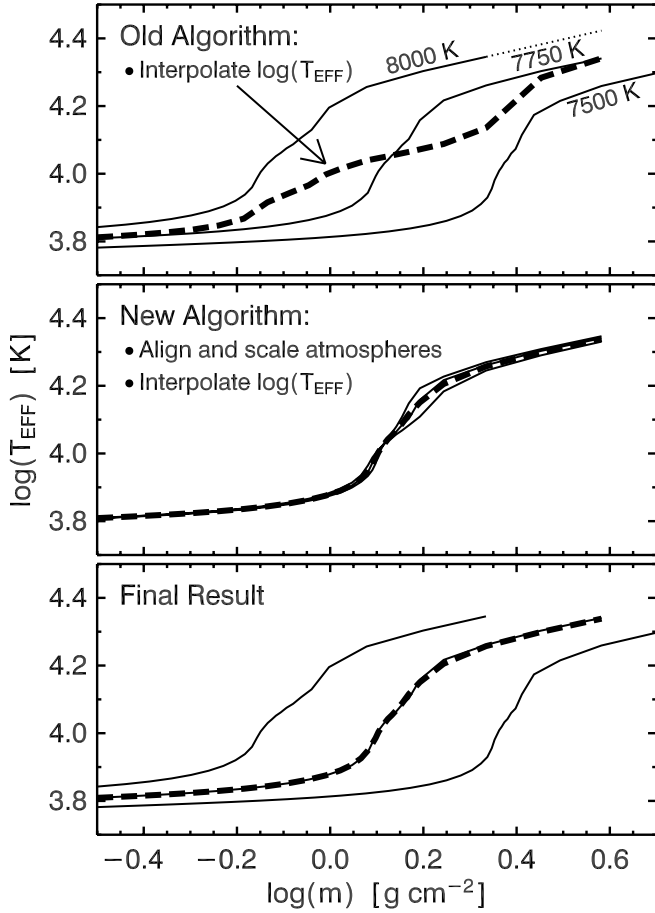


FIG. 2.—Extreme example of the errors that can occur when interpolating in a coarse grid of model atmospheres, without first aligning and scaling the atmospheres being interpolated. The three solid curves are $\log g = 4.0$, $[M/H] = 0.0$, Kurucz models. The dashed curves were calculated by interpolating the $T_{\text{eff}} = 7500$ and 8000 K models. The new algorithm more accurately reproduces the actual $T_{\text{eff}} = 7750$ K model. [See the electronic edition of the *Journal* for a color version of this figure.]

we adopted a solar iron abundance of $\log \epsilon(\text{Fe}) = 7.50$ (e.g., Holweber et al. 1991). When calculating the opacities needed for spectral synthesis of individual stars, we added $[M/H]$ to our adopted solar abundances for elements heavier than He and independently tuned the abundances of Na, Si, Ti, Fe, and Ni. Using $[M/H]$ to interpolate in a grid of model atmospheres yields atmospheres consistent with our adopted metallicities, except that Kurucz (1992) assumed a solar iron abundance of $\log \epsilon(\text{Fe}) = 7.67$ when constructing the grid. We neglect atmospheric changes due to deviations from a scaled solar abundance pattern.

4.2. Microturbulence

Microturbulence (v_{mic}) is an ad hoc parameter originally introduced to reconcile predicted and observed equivalent widths as a function of line strength, as discussed by Mihalas (1978). Microturbulence is not necessarily required in three-dimensional convective models (Asplund et al. 2000), but v_{mic} is now a standard parameter in one-dimensional analyses of solar-type stars. Because the ad hoc v_{mic} parameter suppresses model deficiencies, v_{mic} could in principle be a function of ionic species, excitation energy, depth of formation, effective temperature, surface gravity, etc.

In a traditional abundance analysis based on line equivalent widths, v_{mic} is adjusted to remove any trend in abundance for

individual atomic transitions as a function of lower excitation potential. In contrast, our spectrum fitting technique uses all available constraints to obtain a single abundance estimate for each element of interest, so we cannot directly use the traditional procedure to set v_{mic} .

In principle, we could let v_{mic} be a free parameter while fitting each spectrum and then adopt the value that minimizes χ_r^2 . We evaluated this possible approach using a large subset of our full sample. The test yielded strongly correlated values of v_{mic} and $[M/H]$, suggesting that v_{mic} and $[M/H]$ are partially degenerate. Based on this result, we decided to fix v_{mic} to minimize errors in $[M/H]$. Despite some contrary results in the traditional literature, v_{mic} itself showed no significant dependence on T_{eff} . Consequently, we decided to adopt $v_{\text{mic}} = 0.85 \text{ km s}^{-1}$ for all stars in our analysis of the full sample.

4.3. Line Broadening Kernels

Spectra of the resolved surface of the Sun reveal velocity fields that vary by a few km s^{-1} , due to granulation and acoustic oscillations driven by subsurface convection. High-resolution spectra demonstrate that analogous velocity fields are ubiquitous in cool stars with convective envelopes. For unresolved stars, it is common to characterize these motions as macroturbulence with equal amplitudes (v_{mac}) for separate radial and tangential motions. We ignore changes in the velocity field with depth into the stellar atmosphere, which cause significant asymmetries in observed line profiles (Valenti & Piskunov 1996). Physical models of granulation have been explored in three-dimensional hydrodynamical simulations (e.g., Asplund et al. 2000), but the results have not yet been distilled into a formulation suitable for use in one-dimensional models.

The Sun also has a systematic velocity gradient across the surface due to rotation, with zero velocity on the rotational axis and maximum velocity ($v \sin i$) where the equator intersects the limb. We assume the entire stellar surface rotates uniformly, ignoring surface differential rotation, which has a negligible effect on the shapes of line profiles in slowly rotating stars.

Macroturbulence, rotation, and the instrumental profile all broaden spectral lines without altering their equivalent width. We used an annular disk integration algorithm to combine intensity spectra at 7μ values into a flux spectrum of the star as a whole. We convolve the intensity spectrum for each annulus on the stellar surface with one kernel that describes the distribution of rotational velocities in the annulus and two separate kernels that describe characteristic radial and tangential macroturbulent motions, projected onto the line of sight. This annular disk integration algorithm treats limb darkening explicitly by reference to synthesized intensity spectra at several μ values, rather than assuming a function form. Finally, we convolve the intrinsic flux spectrum of the star by the instrumental profile to simulate the observed spectrum.

Distinguishing between macroturbulence, rotation, and instrumental broadening is difficult in echelle spectra of slowly rotating cool stars because all of these broadening mechanisms are comparable to intrinsic line widths, which are a few km s^{-1} , so we used separate calibration spectra to characterize instrumental broadening (§ 2.3).

4.4. Macroturbulence Relationship

Because v_{mac} seems to vary systematically across the Hertzsprung-Russell (HR) diagram (Gray 1988), adopting a global macroturbulence relationship should yield more accurate results than solving for v_{mac} in each individual spectrum. Initially, we tried using the global macroturbulence relationships in Gray (1988) and

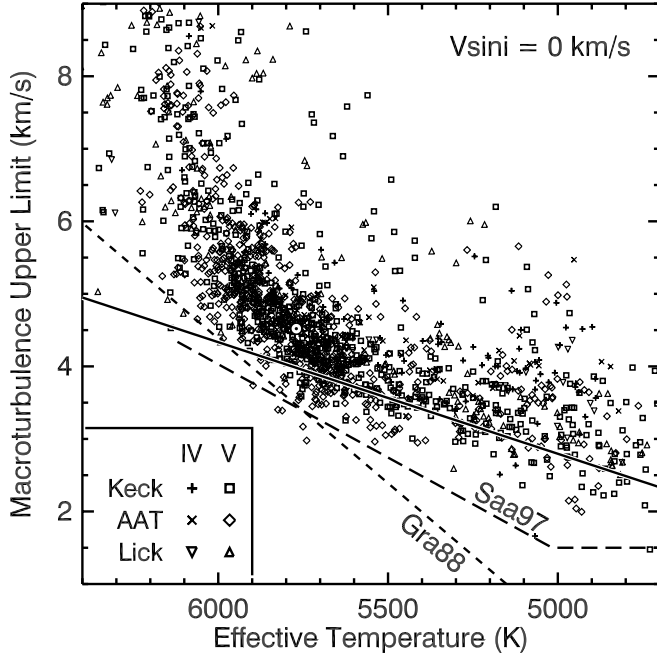


FIG. 3.—Upper limits on macroturbulence as a function of T_{eff} , obtained by setting $v \sin i = 0$ and solving for v_{mac} . Symbol types indicate where the observation was obtained and whether the star is on or slightly above the main sequence. The location of the Sun is indicated. Our adopted relationship between v_{mac} and T_{eff} (eq. [1]) is shown as a solid line. Analogous relationships from Gray (1988) and Saar & Osten (1997) are also shown. [See the electronic edition of the Journal for a color version of this figure.]

Saar & Osten (1997), but these tests yielded implausible $v \sin i$ distributions for our sample. If correct, the $v \sin i$ distributions would imply that most stars in our sample have equatorial velocities of at least 3 km s^{-1} , which is inconsistent with measured rotation periods for inactive field stars (Noyes et al. 1984). The velocity at the solar equator is about 2 km s^{-1} , but because we neglect differential rotation in our spectrum synthesis, solar line profiles are better described by an effective equatorial velocity of approximately 1.6 km s^{-1} (Valenti & Piskunov 1996). This solar $v \sin i$ value depends on the assumed functional form of macroturbulence and the adopted value of v_{mac} .

Given the preceding result, we decided to redetermine the relationship between spectral type and position in the HR diagram. We set $v \sin i = 0 \text{ km s}^{-1}$ and solved for v_{mac} , holding all other parameters fixed. This procedure yielded an upper limit on the true macroturbulence because the v_{mac} parameter was used to characterize (imperfectly) the effects of both rotation and macroturbulence. Figure 3 shows the resulting upper limits, which vary systematically with T_{eff} . We achieve consistent results for spectra from all three observatories, demonstrating that our treatment of instrumental profiles (§ 2.3) is probably adequate.

Below 5800 K, we believe that the lower envelope in Figure 3 is defined by stars with negligible $v \sin i$. For these stars, setting $v \sin i = 0 \text{ km s}^{-1}$ yielded the actual macroturbulence, rather than an upper limit. Visual inspection of Figure 3 yielded an approximate envelope slope of 1 km s^{-1} per 650 K, with hotter stars having higher photospheric velocities, perhaps due to higher subsurface convective velocities. We forced $v_{\text{mac}} = 3.98 \text{ km s}^{-1}$ at $T_{\text{eff}} = 5770 \text{ K}$, so that $v \sin i = 1.63 \text{ km s}^{-1}$ for the Sun, obtaining

$$v_{\text{mac}} = \left(3.98 - \frac{T_{\text{eff}} - 5770 \text{ K}}{650 \text{ K}} \right) \text{ km s}^{-1}. \quad (1)$$

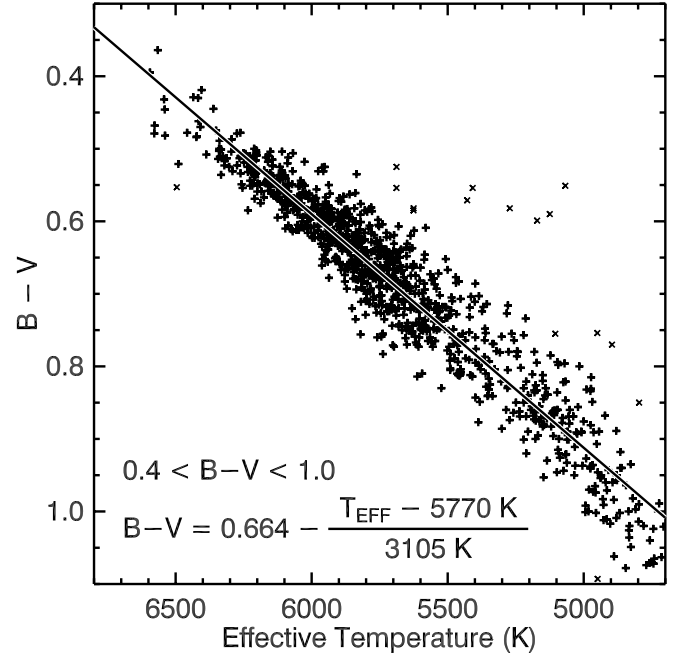


FIG. 4.—Literature values of $B - V$ color as a function of our T_{eff} , along with a linear fit obtained by iteratively rejecting outliers (crosses) with $B - V$ residuals larger than 0.13 mag. [See the electronic edition of the Journal for a color version of this figure.]

Some stars with low $v \sin i$ appear below the envelope due to measurement errors. In contrast, stars with significant $v \sin i$ correctly appear above the lower envelope. We do not detect a statistically significant difference between velocities in dwarf and subgiants.

Above 5800 K, the locus of points in Figure 3 rises sharply above our linear macroturbulence relationship in equation (1). Our relationship assumes this rise is due solely to an increase in the mean rotation rate of hotter stars, but some or all of the rise may be due to macroturbulence instead. It might be possible to test this hypothesis by examining the distribution of $v \sin i$ values in an unbiased sample or by modeling line asymmetries. If we have underestimated v_{mac} above 5800 K, then we will overestimate $v \sin i$, especially when $v \sin i$ is near zero.

Figure 3 also shows the macroturbulence relationships of Gray (1988) and Saar & Osten (1997), expressed in terms of our T_{eff} , rather than $B - V$ (see below). These two relationships adopt the same v_{mac} for the Sun but have different slopes. Both are steeper than our relationship, given in equation (1), possibly because Gray (1988) and Saar & Osten (1997) considered stars at higher T_{eff} , where the locus of points in Figure 3 is no longer linear. As discussed above, we may indeed be underestimating the increase in v_{mac} with temperature above 5800 K, but below this threshold the data require our adopted slope. Although our spectra are slightly lower resolution than those used in Gray (1988) and Saar & Osten (1997), we certainly have many more stars that can be used to assess uncertainties, and the I_2 analysis may yield a more accurate instrumental profile.

Gray (1988) and Saar & Osten (1997) express v_{mac} in terms of $B - V$, rather than T_{eff} . For our sample, the mean relationship between $B - V$ and T_{eff} is

$$B - V = 0.664 - \frac{T_{\text{eff}} - 5770 \text{ K}}{3105 \text{ K}}, \quad (2)$$

over the range $0.4 < B - V < 1.0$. Figure 4 shows that there is significant scatter about this mean relationship, presumably due

to differences in $[M/H]$ and perhaps extinction in some cases. Empirically, we find that the lower envelope in Figure 3 becomes less distinct when v_{mac} is plotted versus $B - V$, rather than T_{eff} . Physically, this suggests that v_{mac} is controlled more directly by energy flux at the surface, rather than broad band colors. This is plausible because v_{mac} is an indirect manifestation of (convective) energy flux just below the photosphere, while T_{eff} is a measure of the same energy flux (now radiative) in the photosphere. We advocate expressing v_{mac} in terms of T_{eff} , rather than $B - V$.

5. FITTING OBSERVED SPECTRA

5.1. Free Parameters

We configured SME to fit each stellar spectrum by adjusting a total of 41 free parameters: 9 global parameters that affect the entire spectrum and 4 local parameters for each of the 8 distinct wavelength intervals. The global parameters were T_{eff} , $\log g$, $[M/H]$, $v \sin i$, and the abundances Na, Si, Ti, Fe, and Ni. The $[M/H]$ parameter is used to interpolate in the grid of model atmospheres and to scale the solar abundance pattern (except for helium and the five elements just mentioned) when calculating opacities. The $[M/H]$ parameter is an independent model parameter, rather than a quantity constructed from individual abundances.

The local parameters for each wavelength interval consisted of 3 quadratic polynomial coefficients used to correct the continuum normalization and one velocity offset used to correct the radial velocity. We enhanced SME to allow the continuum correction to be quadratic, rather than linear. For most stars, we applied a separate velocity correction to each wavelength interval to minimize the effect of wavelength calibration errors on our derived stellar parameters. We used the mean of the velocity corrections for all 8 wavelength intervals to generate our final radial velocity. For 35 spectra of very cool or metal-poor stars, SME was unable to obtain a reliable velocity correction for one or more segments. In these few cases, we configured SME to apply a single global velocity correction to all 8 wavelength intervals, requiring a total of 34 free parameters.

5.2. Methodology

SME uses the Levenberg-Marquardt (LM) algorithm to solve the nonlinear least-squares problem of fitting an observed spectrum with a synthetic spectrum. The LM algorithm combines gradient search and linearization methods to locate efficiently parameter values that yield a χ^2 value close to the minimum. Additional improvement is inefficient, so the LM algorithm terminates with parameter values that are nearly optimal. Deviations from the optimal solution depend on the specific choice of initial parameter values, but not in a systematic way.

SME only uses the LM algorithm to optimize global parameters (9 in our case). The remaining local parameters (4 per wavelength interval in our case) are optimized separately each time the LM algorithm calls the function that generates a synthetic spectrum. The spectrum synthesis function determines the optimum velocity shift using a one-dimensional golden section search. For each velocity shift considered, SME solves a linear least-squares problem to determine the best continuum fit. In other words, SME uses three nested algorithms to fit an observed spectrum.

A mask specifies which “line” pixels should be used to determine velocity shifts and calculate χ_r^2 , and which “continuum” pixels should be used to determine quadratic continuum adjustments. The presence of spectral lines in “continuum” windows will not adversely affect continuum placement, as long as the lines are accurately modeled in the synthetic spectrum. In practice,

we selected continuum windows with a few lines as possible. Figures 5 and 6 indicate typical line and continuum windows for our observed spectra. We used the solar spectrum to define one master mask in terms of laboratory wavelengths and then shifted this mask to the rest frame of each stellar spectrum in order to obtain consistent results. However, minor adjustments were necessary for some stars.

Choosing good initial values for the global free parameters improves the speed and robustness of convergence. We calculated our initial T_{eff} from $B - V$ color, using a relationship similar to equation (2). We based our initial value of $\log g$ on generic main-sequence masses (Cox 2000) and radii calculated as described in § 7.2, but with our initial estimates of T_{eff} . We started with $v \sin i = 0.5 \text{ km s}^{-1}$, $[M/H] = 0$, and solar abundances for Na, Si, Ti, Fe, and Ni.

Negative values of $v \sin i$ are not physically meaningful, so we added logic to SME that temporarily treats $v \sin i$ like a fixed parameter, rather than letting the LM algorithm step to a negative value of $v \sin i$. Also, we had to redetermine $v \sin i$ after solving for all the other free parameters because we updated our measurements of resolution (see § 2.3) and our v_{mac} formulation (see § 4.4). These two changes affected only the line broadening kernels and not line strength, so we were able to start with the specific intensity profiles from the initial analysis, avoiding the need to repeat the radiative transfer calculations. We reran the full analysis for 100 randomly selected spectra to validate this procedure.

5.3. Computer Resources

Fitting one spectrum took a CPU hour on the fastest workstation available to us (2 GHz Power Mac G5) and up to 7 times longer on progressively slower workstations. We used 50 CPUs to fit 1955 spectra in 5400 CPU hours, not counting the extensive additional time required to develop and test our analysis technique. The external C++ library (opacities, radiative transfer) used 94% of the CPU time, compared to 6% used by IDL. Fitting one spectrum typically required 6 iterations of the LM algorithm and 80 spectrum synthesis calculations.

6. ERROR ANALYSIS

In this section we describe systematic corrections that we applied to our raw results from SME to match known solar properties, yield consistent abundances within binaries, and remove abundance trends with T_{eff} . At the same time, we characterize the general precision of our spectroscopically determined stellar parameters.

6.1. Vesta Correction

In § 3.3 we used a solar spectrum to solve for empirical line data corrections, keeping stellar parameters fixed at known solar values. In this section we employ our stellar analysis technique on spectra of the Sun, keeping the line data fixed and solving for solar parameters. We compare our derived solar parameters with known values to evaluate the precision and accuracy of our analysis technique and to determine empirical corrections for our stellar parameters.

To properly assess errors related to our data handling procedures, we analyzed solar spectra obtained in the same manner as our stellar spectra. Specifically, we analyzed observations of the asteroid Vesta, which reflects the solar spectrum and has a brightness comparable to our stellar targets. We analyzed 3 Keck spectra of Vesta obtained consecutively on 1997 August 6, and 3 more spectra obtained on 2004 June 25, bracketing the time period when most of the stellar observations were obtained.

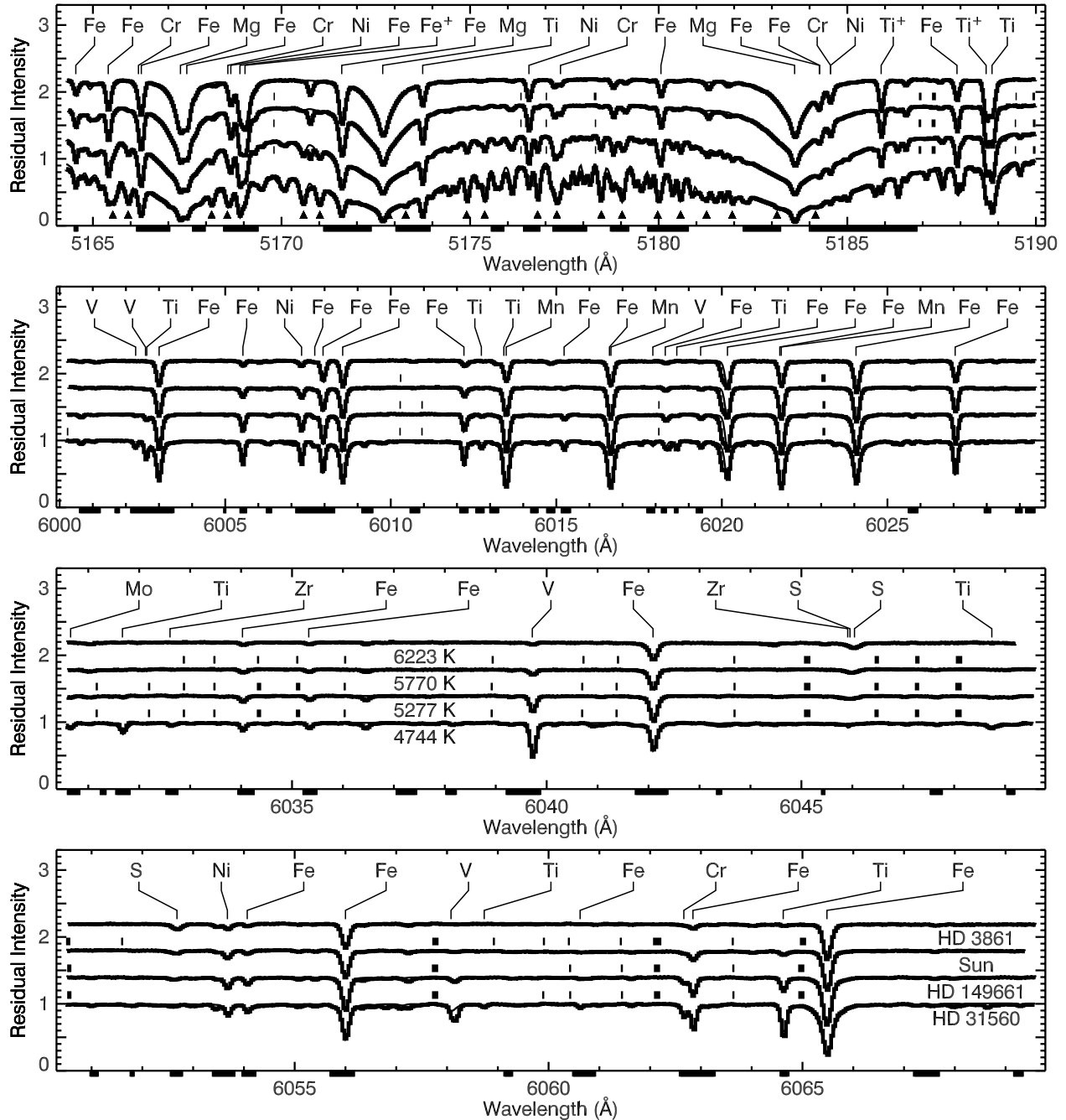


FIG. 5.—Observed and overplotted synthetic spectra for the first four wavelength intervals. The four stars in each panel span the range of T_{eff} in our sample. Bold horizontal line segments along the bottom axis demarcate spectral segments used to constrain synthetic spectrum fits. [See the electronic edition of the Journal for a color version of this figure.]

As noted in § 5.2, free parameters converge to final values that depend to some extent on the initial values. More precise results may be obtained by repeating the analysis with many initial parameter values and then averaging the results. This was not practical for all of our 1944 spectra, but we did analyze each of our 6 Vesta spectra with 81 different sets of initial parameter values. We changed the initial T_{eff} by ± 100 K, $\log g$ by ± 0.1 , $[M/H]$ by ± 0.2 , and $v \sin i$ by ± 1.1 km s $^{-1}$, yielding a total of $4^3 = 81$ combinations. In all cases, individual elemental abundances began at solar values.

Figure 7 shows the distribution of final parameter values for 81 different sets of initial values, used to analyze 6 spectra of Vesta obtained on two different observing runs. The electronic ver-

sion of the Journal includes a color version of the figure that also shows separate distributions for each of the 6 spectra. These roughly Gaussian distributions for individual spectra demonstrate the sensitivity of final parameter values to different initial values, characterizing the imperfect numerical convergence of the LM algorithm. Table 4 gives the standard deviation (σ_i) of final parameter values about the mean for each observation, due only to differences in initial values.

Averaging results for the 81 different initial parameter values yields a more precise mean result for each observation. Table 4 gives the standard deviation (σ_o) of these precise means for each observation about the global mean (m) for all 6 observations, characterizing the component of measurement error that changes

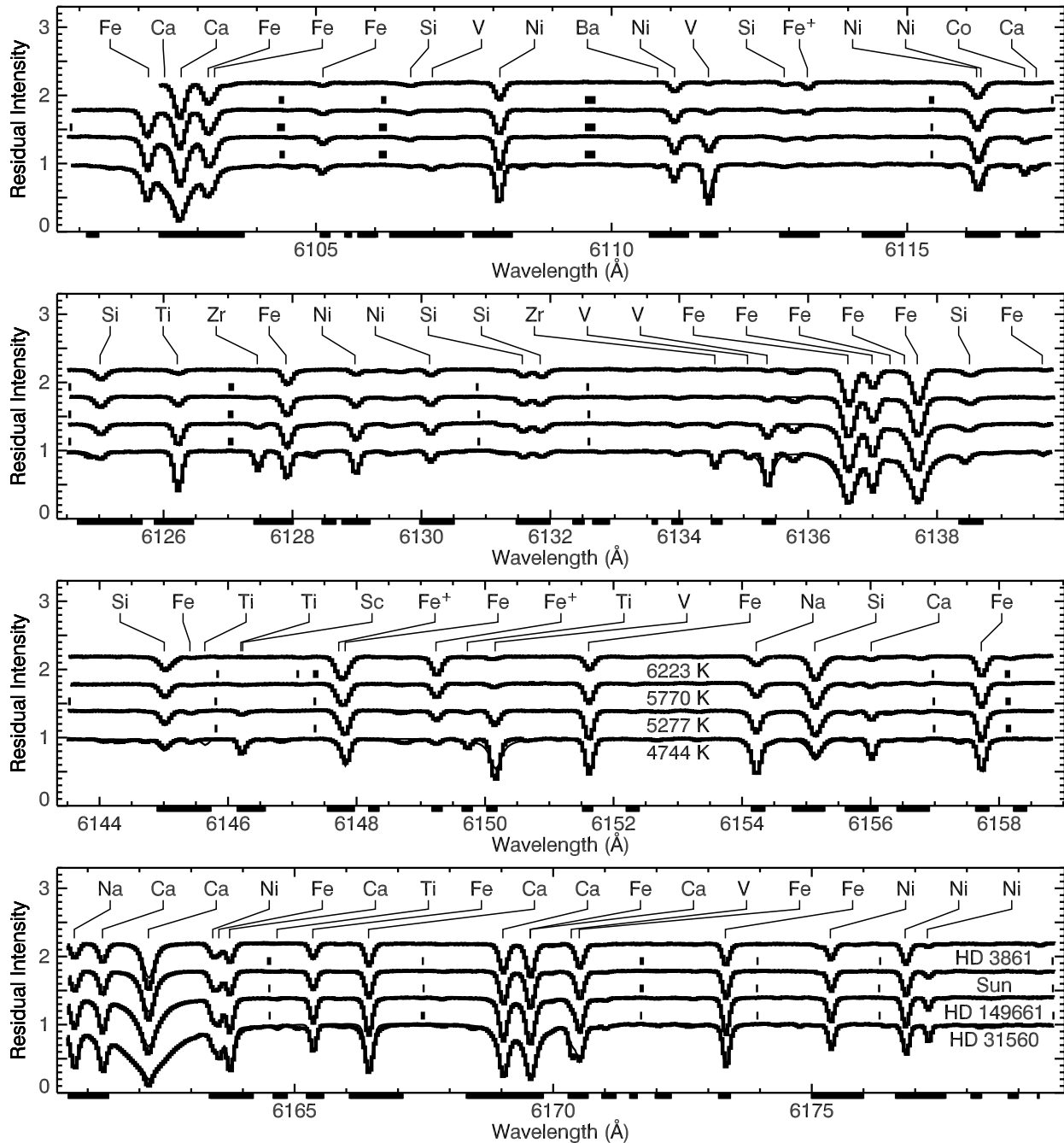


FIG. 6.—Same as Fig. 5, except for the second set of four wavelength intervals. [See the electronic edition of the *Journal* for a color version of this figure.]

with each observation. We do not have enough observations of Vesta to assess whether errors are distributed normally or to separate long-term errors from variations in consecutive spectra.

Comparing σ_i with σ_o for T_{eff} and $v \sin i$ illustrates the distinction between these two types of error. Random errors in T_{eff} are dominated by imperfect numerical convergence ($\sigma_i > \sigma_o$), whereas random errors in $v \sin i$ are dominated by measurement errors ($\sigma_i < \sigma_o$). The color version of Figure 7 shows this graphically; the individual distributions for each parameter all overlap for T_{eff} , but not for $v \sin i$. As discussed in § 2.3, low values of $v \sin i$ are particularly sensitive to changes in the instrumental profile.

In addition to characterizing individual error components, we also calculated the overall standard deviation (σ) about the global mean (m) for each derived parameter. The results appear

in Table 4. These values are one estimate of the expected uncertainties in our final parameters, when analyzing a single observation with only one set of initial parameter values. Note that each σ is approximately equal to the corresponding uncertainty components, σ_i and σ_o , added in quadrature.

Finally, Table 4 gives the overall mean (m) and the associated uncertainty (σ_m) for each derived parameter. Results for the 486 trials are not independent because they are based on only 6 Vesta observations, so $\sigma/\sqrt{486}$ is not a good estimate of σ_m . Instead, we set σ_m equal to the larger of $\sigma_o/\sqrt{6}$ and $\sigma_i/\sqrt{81}$. Table 4 gives m , our adopted σ_m , and the correction (ΔP) that we added to all raw parameter values returned by SME. The correction is relatively small, but errors in our empirical line data (see § 3.3) can compensate for deficiencies in our models (e.g., assuming LTE, one-dimensional, static atmospheres). Indeed, our raw abundances

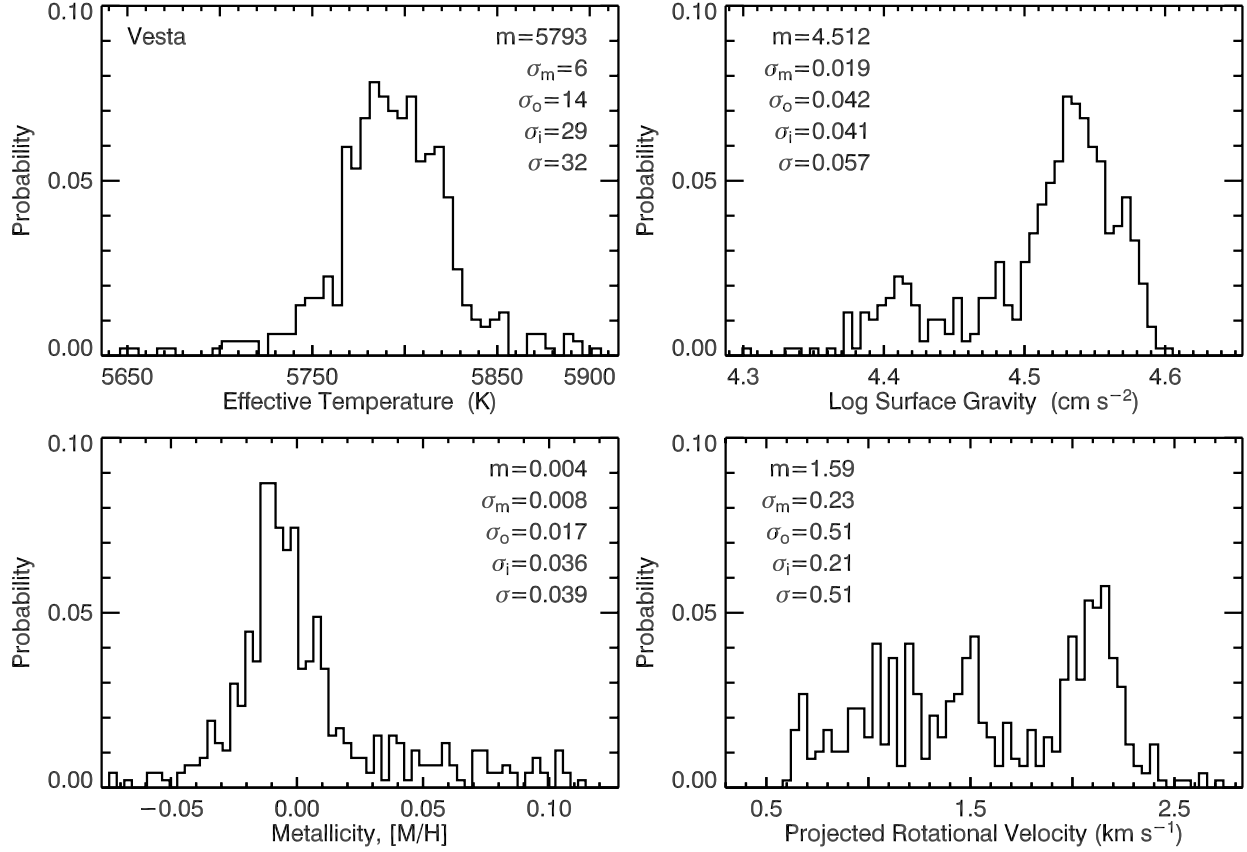


FIG. 7.—Distribution of model parameters for 81 different sets of initial values used to analyze 6 spectra of Vesta. [See the electronic edition of the *Journal* for a color version of this figure.]

vary systematically with T_{eff} , requiring an additional correction as a function of T_{eff} (see § 6.4).

6.2. Root Mean Square Residuals

Figure 8 shows rms residuals as a function of T_{eff} for our synthetic spectrum fits of 1807 observed spectra. Root mean square residuals in our “continuum” windows (see § 5.2) are typically less than 1%, but more than the 0.3% measurement error in each observed pixel, due to the presence of unidentified weak lines. Root mean square residuals in “line” windows are almost twice the residuals in continuum windows, due mainly to errors in line shape at solar temperatures (Valenti & Piskunov 1996) and due to errors in uncorrected data as temperatures deviate from solar. Lines that are too weak in the solar spectrum to constrain empirical line data corrections (see § 3.3) can become strong at warmer or especially cooler temperatures.

After fitting an observed spectrum, SME calculates the formal uncertainty in the final value of each free parameter. This formal uncertainty scales with the measurement uncertainties assigned to pixels in the observed spectrum. Because the typical residual (1.2%) about our best-fitting synthetic spectrum is much larger than the uncertainties (0.3%) in our observed spectrum, the actual uncertainties in our derived parameters are significantly larger than the formal uncertainties returned by SME. Our only recourse is to estimate uncertainties empirically by comparing results for multiple spectra of the same star.

6.3. Random Errors

Our sample included 712 stars with only one observation and 328 stars with multiple observations (typically 3, maximum of 22 for HD 10700). Thus, we can determine empirical uncertainty estimates for a third of our sample, but for the remaining stars, all

TABLE 4
VESTA ERROR ANALYSIS AND PARAMETER CORRECTIONS

Parameter	σ_i	σ_o	σ	m	ΔP
T_{eff} (K)	30	14	33	5793(06)	−23
$\log g$ (cgs).....	0.036	0.042	0.057	4.512(19)	−0.074
[M/H].....	0.020	0.017	0.039	0.004(06)	−0.004
[Na/H].....	0.017	0.021	0.026	−0.057(09)	+0.057
[Si/H].....	0.011	0.006	0.012	−0.019(03)	+0.019
[Ti/H].....	0.029	0.020	0.034	+0.051(09)	−0.051
[Fe/H].....	0.020	0.007	0.021	−0.003(03)	+0.003
[Ni/H].....	0.020	0.010	0.022	−0.007(04)	+0.007
$v \sin i$ (km s ^{−1}).....	0.21	0.51	0.34	1.59(29)	+0.04
v_{rad} (km s ^{−1}).....	0.004	0.56	0.51	−0.12(51)	+0.12

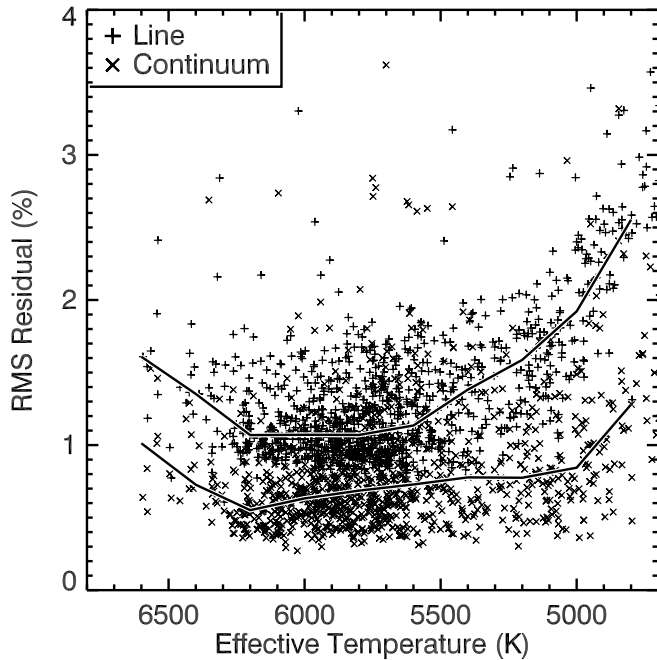


FIG. 8.—Root mean square residuals for continuum (crosses) and line (pluses) pixels, as a function of T_{eff} , based on data in Table 8. Line segments connect median rms residuals in T_{eff} bins with widths of 200 K. The median line rms exceeds the median continuum rms due to errors in line data, nonsolar abundance patterns, non-LTE effects, etc. The median rms increases at extreme temperatures as line blends that are not prominent in the solar spectrum become significant. [See the electronic edition of the Journal for a color version of this figure.]

we can do is assume that they have comparable errors. Because uncertainty estimates for individual stars are imprecise, we combined results for all stars to determine a global uncertainty distribution for each parameter, which we assume applies individually to each star. For normally distributed errors, uncertainty may be characterized by the standard deviation of multiple determinations of the same parameter. However, we had enough redundant measurements to construct an empirical error distribution for each parameter.

Figure 9 shows our empirical error distribution for each stellar parameter. We constructed these distributions by binning parameter differences, divided by $\sqrt{2}$, for every pairwise permutation of results for stars with multiple observations. The $\sqrt{2}$ scaling converts the difference between two measurements into an estimate of the uncertainty in one measurement, assuming both measurements have equal uncertainty. In the electronic version of the Journal, Figure 9 also shows (in color) separate error distributions for the three observing sites. In most cases, the error distributions are statistically equivalent, but very few stars were observed multiple times at Keck.

There are $p = n(n-1)$ pairwise permutations of n measurements for a particular star, but these permutations provide only $n-1$ independent constraints on the error distribution. Thus, we assigned a weight of $(n-1)/p = 1/n$ to the difference associated with each permutation. With this weighting, the area under each error distribution equals the total number of independent constraints for all stars, which may also be characterized as the number of “unique pairs” of measurements. The distributions are symmetric because each unique pair has two permutations that yield differences with equal magnitude, but opposite sign.

Using the error distributions in Figure 9, we determined error thresholds that would include 68.3%, 95.4%, and 99.7% of the unique pairs in our empirical distributions. Table 5 reports these

error thresholds, which correspond to 1, 2, and 3 σ probabilities in a normal distribution. Figure 9 indicates the thresholds graphically. The 95.4% thresholds are generally more than twice the 68.3% thresholds, indicating that the wings of our error distribution are more extended than a normal distribution. We reinforce this point by overplotting on each error distribution a Gaussian fit and tabulating the corresponding 1 σ standard deviation. Our v_{rad} error distribution has particularly broad wings, due to uncorrected wavelength drift throughout the night (see § 2.4) and intrinsic stellar variations in some cases.

Table 6 lists the uncertainties that we adopted for parameters obtained by fitting a single observation of a generic star. To calculate the uncertainty in the mean result for n observations of a specific star, these generic uncertainties should be divided by \sqrt{n} . This formulation may underestimate uncertainties in derived parameters for metal-poor or rapidly rotating stars, which have relatively shallow lines. We obtained the generic uncertainties in Table 6 by adding in quadrature the “68.3%” empirical error thresholds for “all sites” from Table 5 and values of σ_i from Table 4. The first term describes the measurement error in each individual observation, while the second term describes the numerical error caused by using the LM algorithm with only one set of initial values. We then increased the generic uncertainty for $v \sin i$ from 0.31 to 0.5 km s^{-1} and for v_{rad} from 0.12 to 0.3 km s^{-1} to better characterize in a single parameter the non-Gaussian wings (see Fig. 9) of the empirical error distributions for these parameters.

6.4. Spurious Abundance Trends

Our analysis of Vesta spectra (see § 6.1) yielded corrections (ΔP in Table 4) that removed small systematic errors in our raw results for the Sun and presumably other stars with similar T_{eff} . Nonetheless, systematic errors may remain at other T_{eff} , especially in abundances, which are sensitive to departures from LTE excitation and ionization.

We used two assumptions to test for systematic abundance errors at nonsolar T_{eff} . First, we assumed that the ratio of one elemental abundance to another (or to metallicity) does not vary systematically with T_{eff} for our sample as a whole. This ignores any metallicity bias in our warmest stars that might be caused by evolution of an old population off the main sequence. Second, we assumed that stars in a multiple system should be chemically similar by virtue of a common origin. As described below, our raw abundances violated both of these assumptions, so we determined and applied abundance corrections to remove trends with T_{eff} .

If abundances of a reference element are correct for all T_{eff} , then removing the trend in each abundance ratio that involves the reference element corrects any errors in the abundance of the other element. The Sun can then be used to fix the abundance zero point for each element. On the other hand, if all abundances have spurious trends with T_{eff} , then abundance ratios alone do not provide enough constraints to uniquely determine a correction.

Each pair of chemically similar stars that spans a range of T_{eff} provides a constraint on the *slope* of any spurious abundance trend. In principle, the slopes from several pairs of stars can be spliced together to reconstruct the spurious abundance trend. Again the Sun can be used to fix the abundance zero point for each element. In practice, this procedure works only if the slope is large compared to measurement errors or many associated pairs are available. Stars in a cluster would be ideal for this purpose.

Initially, we used both abundance ratios and associated stars to determine spurious trends in $[M/H]$ and our raw abundances for

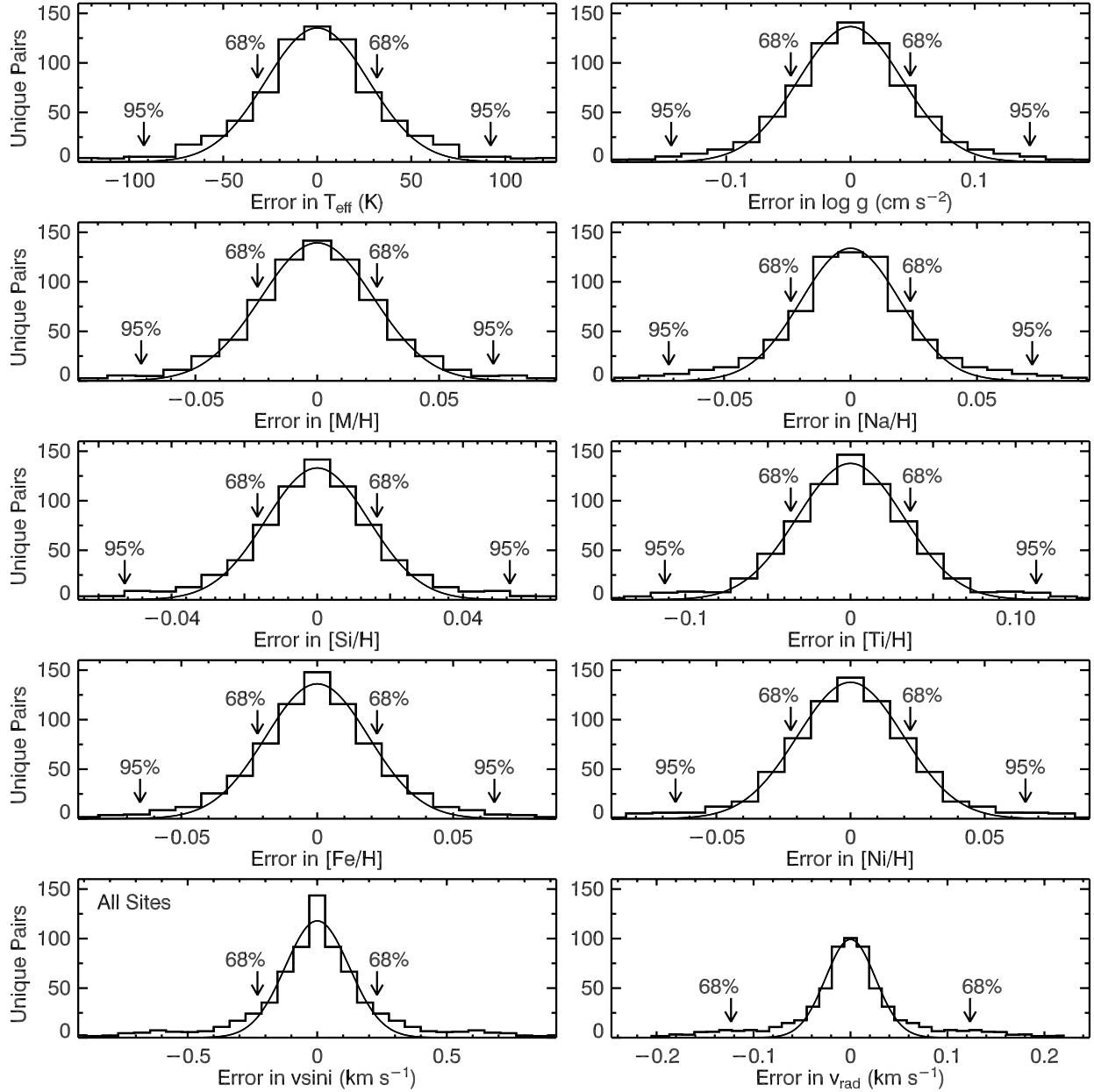


FIG. 9.—Distribution of parameter errors determined by comparing results for multiple spectra of the same star. The wings are more extended than a normal distribution, as illustrated by the overlapped Gaussian profile. We label points in the error distributions that enclose 68% and 95% of each distribution, corresponding roughly to 1 and 2 σ confidence levels. The error distribution for v_{rad} has particularly broad wings, due to uncorrected wavelength drift throughout the night. Below the summed distribution for all observatories, separate distributions for each observatory are shown. [See the electronic edition of the *Journal* for a color version of this figure.]

Na, Si, Ti, Fe, and Ni. However, our measurement errors were large enough that the solution was not robust against minor changes in the constraints. The trend in $[M/H]$ with T_{eff} was relatively small, perhaps because $[M/H]$ is also used to select the model atmosphere. Therefore, we adopted $[M/H]$ as a reference species and solved for abundance corrections as a function of T_{eff} . Because our sample is so large, abundance ratios for all stars provided a stronger constraint than matching abundances in two dozen pairs of stars, even though the composition of the sample as a whole is heterogeneous.

We used the results of this trend analysis to correct our raw abundances of Na, Si, Ti, Fe, and Ni. Table 7 gives the amount that we would have subtracted from our raw abundances for a few illustrative T_{eff} . Errors of this magnitude would be difficult to detect in a smaller sample, unless the stars were all chemically

homogeneous. We assumed that abundance trend corrections are zero at $T_{\text{eff}} = 5770$ K, after applying zero-point corrections from the Vesta analysis. This assumption neglects the possibility that the Sun itself may have peculiar abundances (e.g., Allende Prieto et al. 2004).

The remainder of this section is primarily a description of Figures 10 and 11, which illustrate the analysis procedure just described. The top row shows the ratio of our raw elemental abundances to metallicity for every star in our sample (*small dots*). Let $[\epsilon/M] = [\epsilon/H] - [M/H]$, where ϵ represents any one of the elements Na, Si, Ti, Fe, or Ni. The median $[\epsilon/M]$ in 200 K bins (*large crosses*) exhibits different trends with T_{eff} for each element. We excluded other abundance ratios (e.g., $[\text{Fe}/\text{Ni}]$) from our analysis because they are degenerate with the $[\epsilon/M]$ set. Each panel shows the abundance corrections we determined,

TABLE 5
UNCERTAINTY ANALYSIS FOR STARS WITH MULTIPLE SPECTRA

CONFIDENCE		T_{eff}	$\log g$	[M/H]	[Na/H]	[Si/H]	[Ti/H]	[Fe/H]	[Ni/H]	$v \sin i$	v_{rad}
Limit	Type ^a	(K)	(cm s^{-2})							(km s^{-1})	(km s^{-1})
All Sites: 328 Stars, 744 Constraints, ^b 1072 Spectra, 3070 Permutations ^c											
68.3%	Empir.	32	0.048	0.025	0.024	0.016	0.036	0.022	0.022	0.23	0.12
95.4%	Empir.	92	0.144	0.072	0.072	0.053	0.112	0.065	0.065	1.05	0.77
99.7%	Empir.	233	0.355	0.199	0.182	0.122	0.264	0.218	0.164	2.08	1.56
1 σ	Gauss	27	0.042	0.023	0.020	0.014	0.032	0.019	0.020	0.12	0.03
Keck only: 7 Stars, 14 Constraints, 21 Spectra, 56 Permutations											
68.3%	Empir.	26	0.063	0.015	0.012	0.010	0.023	0.012	0.017	0.41	0.50
95.4%	Empir.	62	0.116	0.027	0.042	0.020	0.052	0.038	0.027	0.71	0.78
99.7%	Empir.	69	0.138	0.035	0.046	0.021	0.070	0.048	0.032	0.72	0.80
1 σ	Gauss	28	0.053	0.016	0.011	0.013	0.017	0.008	0.005	0.41	0.11
AAT only: 235 Stars, 553 Constraints, 788 Spectra, 2214 Permutations											
68.3%	Empir.	28	0.042	0.021	0.021	0.015	0.034	0.020	0.020	0.22	0.08
95.4%	Empir.	73	0.120	0.066	0.059	0.047	0.093	0.051	0.053	1.02	0.45
99.7%	Empir.	166	0.319	0.149	0.108	0.095	0.171	0.128	0.105	2.05	1.19
1 σ	Gauss.	27	0.038	0.021	0.018	0.013	0.031	0.018	0.019	0.11	0.02
Lick only: 86 Stars, 174 Constraints, 260 Spectra, 784 Permutations											
68.3%	Empir.	50	0.070	0.037	0.037	0.024	0.046	0.034	0.027	0.24	0.25
95.4%	Empir.	134	0.200	0.089	0.106	0.075	0.219	0.092	0.086	1.12	1.29
99.7%	Empir.	242	0.423	0.239	0.215	0.129	0.276	0.231	0.181	2.14	1.72
1 σ	Gauss	33	0.061	0.031	0.030	0.018	0.038	0.025	0.025	0.14	0.06

^a Empir. = Empirical error distribution, Gauss = Normal distribution.

^b There are $n - 1$ constraints for n spectra.

^c There are $n(n - 1)$ pairwise permutations.

which were cubic polynomials. A horizontal dashed line at zero indicates the solar value of $[\epsilon/\text{M}]$. The second row repeats data from top row, but with the cubic polynomial trend removed. We note that [Si/M], [Ti/M], and [Fe/M] for the Sun are 0.024 ± 0.003 below the median for stars in our sample near $T_{\text{eff}} = 5770$ K in both our raw and corrected abundances.

The third row shows abundances for every associated pair of stars in our sample, with a line segment connecting members of each pair. A preponderance of either positive or negative slopes (see [Fe/H], for example) would indicate a systematic trend in our raw abundances as a function of T_{eff} . We searched our sample for associated pairs of stars that are likely to have a common origin by

TABLE 6
ADOPTED UNCERTAINTIES

Parameter	$\sqrt{n} \sigma^a$
T_{eff}	44 K
$\log g$	0.060 cm s^{-2}
[M/H]	0.029
[Na/H]	0.032
[Si/H]	0.019
[Ti/H]	0.046
[Fe/H]	0.030
[Ni/H]	0.030
$v \sin i$	0.5 km s^{-1}
v_{rad}	0.3 km s^{-1}

^a Divide the tabulated quantity by the square root of the number of measurements (n) to get uncertainty in the mean (σ).

virtue of similar coordinates, distances, proper motions, and radial velocities. We identified 24 associated pairs in previously known systems and apparently discovered that HD 13507 and HD 13531 are associated now or were recently, despite being separated by $53'$ (0.40 pc at distance of 26 pc). Both stars are similar to the Sun, but with ages less than about 2 Gyr based on isochrones (§ 7.2). Precise radial velocity measurements indicate that HD 13507 also has a close companion (Perrier et al. 2003). Pairs with large differences in T_{eff} provide stronger constraints on abundance corrections, so we retained HD 131156 B in our abundance trend analysis, even though it is too cool ($T_{\text{eff}} = 4592$ K) to be in our main sample.

The fourth row repeats data from the third row, but with the mean $[\epsilon/\text{M}]$ for each pair subtracted to create the “ R_1 ” residual, which overlays the line segments without altering their slope. The fifth row shifts the mean $[\epsilon/\text{M}]$ for each pair onto our adopted abundance trend. The bottom row shows the “ R_2 ” residuals, which are the data from the fifth row minus the abundance trend.

TABLE 7
ABUNDANCE TREND CORRECTIONS

T_{eff} (K)	[Ni/H]	[Fe/H]	[Ti/H]	[Si/H]	[Na/H]
4700	−0.030	−0.066	−0.111	0.190	0.051
5200	−0.064	−0.054	−0.049	0.036	−0.029
5770	0.000	0.000	0.000	0.000	0.000
6200	0.017	0.061	0.063	0.020	−0.015
6700	−0.111	0.147	0.210	0.039	−0.206

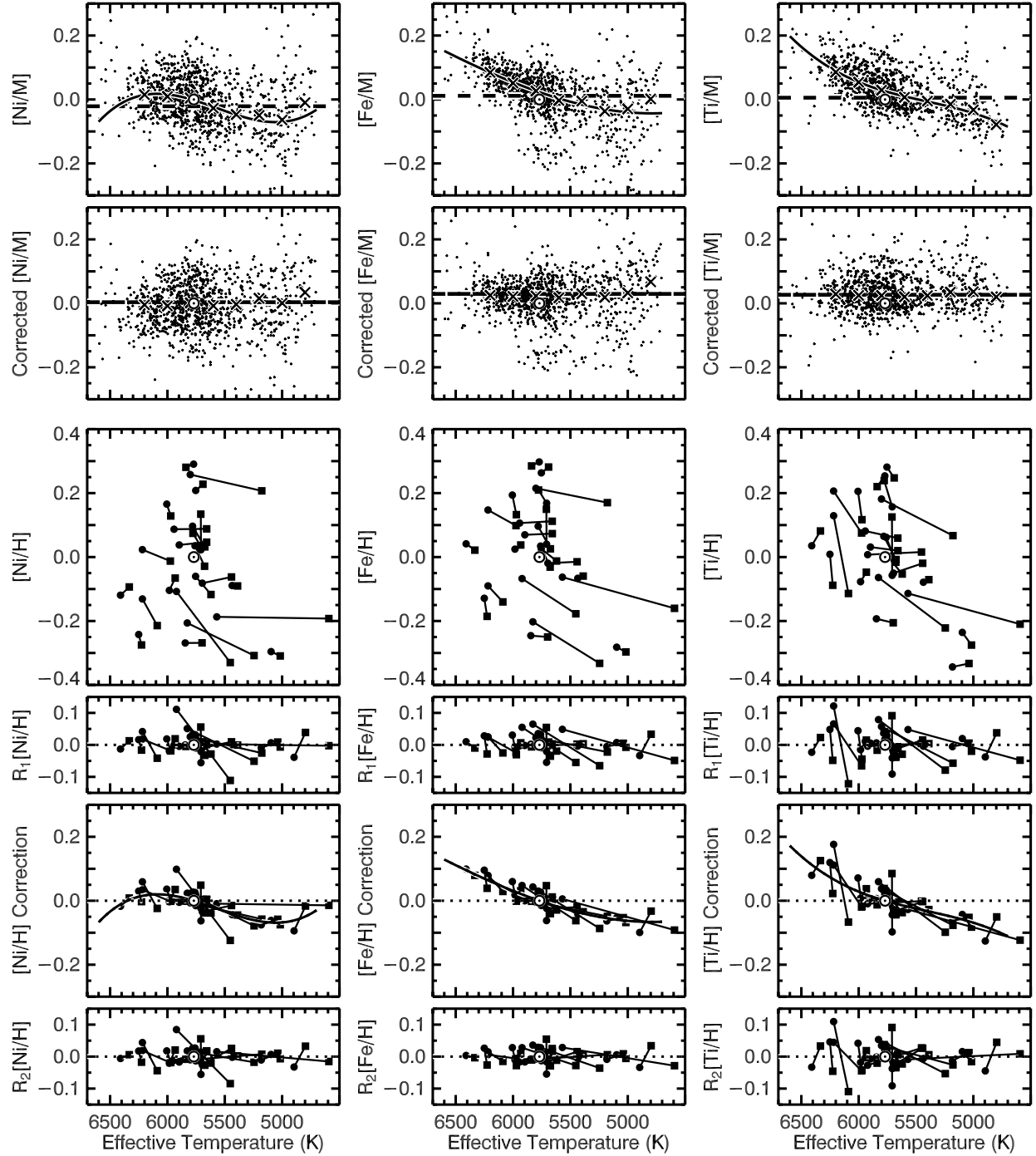


FIG. 10.—Illustration that our abundance corrections remove the mean trends in abundance ratios and balance the number of binaries with abundances that increase or decrease with increasing T_{eff} . Temperature-dependent trends (*top row*) in the abundance ratios $[\text{Ni}/\text{M}]$, $[\text{Fe}/\text{M}]$, and $[\text{Ti}/\text{M}]$ for all stars in our sample are removed (*second row*) after applying polynomial abundance corrections. Linked $[\text{Ni}/\text{H}]$, $[\text{Fe}/\text{H}]$, and $[\text{Ti}/\text{H}]$ abundances for pairs of stars in binaries before (*third row*) and after (*fourth row*) subtracting systemic means are adjusted to show temperature-dependent trends before (*fifth row*) and after (*sixth row*) applying polynomial abundance corrections. [See the electronic edition of the Journal for a color version of this figure.]

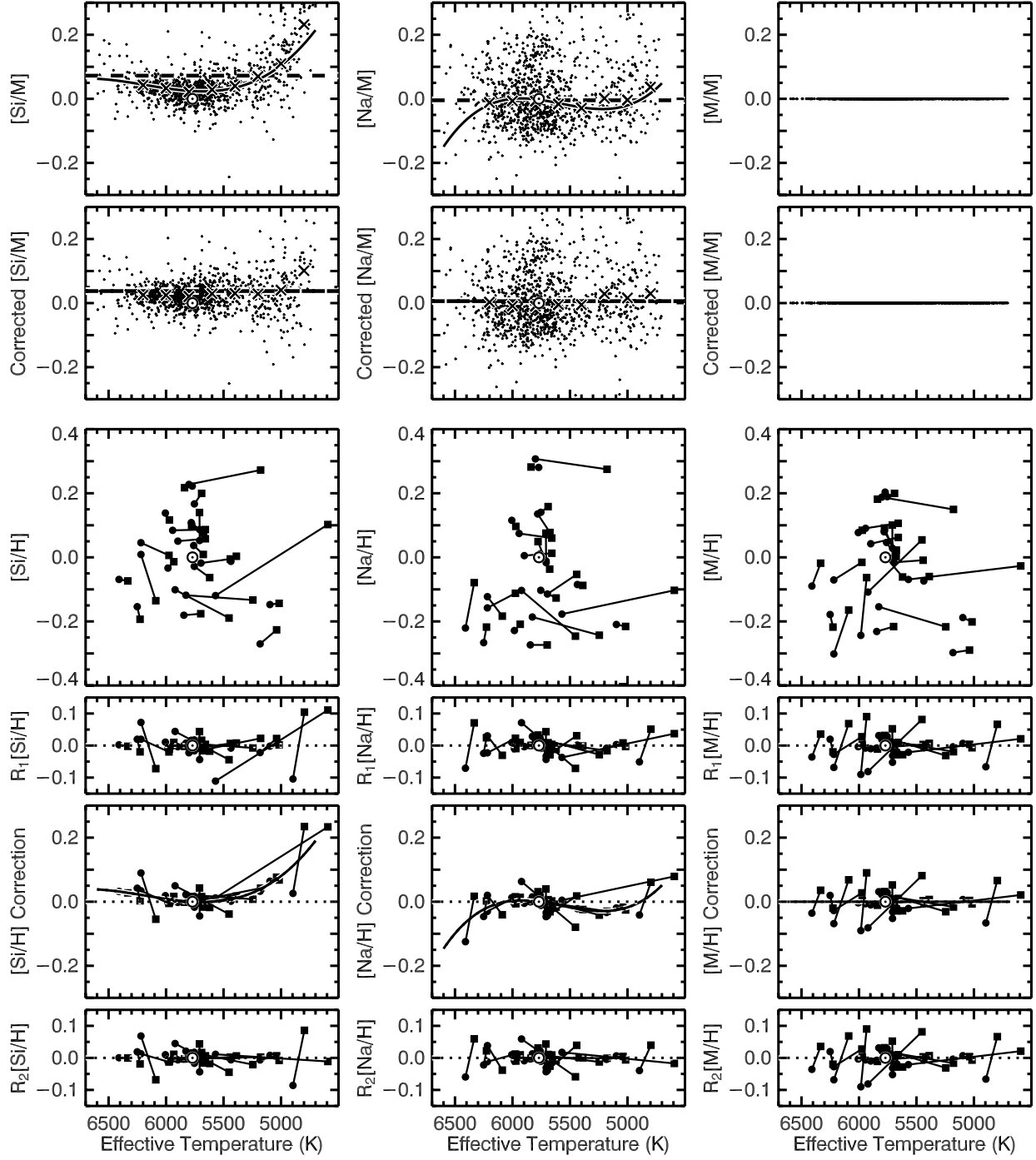


FIG. 11.—Same as Fig. 10, except for $[\text{Si}/\text{M}]$ and $[\text{Na}/\text{M}]$ abundance ratios and $[\text{Si}/\text{H}]$, $[\text{Na}/\text{H}]$, and $[\text{M}/\text{H}]$ abundances in binaries. No correction is applied to $[\text{M}/\text{H}]$. [See the electronic edition of the Journal for a color version of this figure.]

TABLE 8
SPECTROSCOPICALLY DETERMINED STELLAR PROPERTIES

ID (1)	Name (2)	T_{eff} (K) (3)	$\log g$ (cm s^{-2}) (4)	[M/H] (5)	[Na/H] (6)	[Si/H] (7)	[Ti/H] (8)	[Fe/H] (9)	[Ni/H] (10)	$v \sin i$ (km s^{-1}) (11)	v_{rad} (km s^{-1}) (12)	C-rms (13)	L-rms (14)	K (15)	A (16)	L (17)
0.....	Sun	5770	4.44	0.00	0.00	0.00	0.00	0.00	0.00	1.7	-0.1	1.80	1.09	6	0	0
1.....	HD 225261	5265	4.59	-0.31	-0.35	-0.25	-0.28	-0.44	-0.43	0.0	7.7	0.57	1.12	1	0	0
2.....	HD 105	6126	4.65	-0.02	-0.20	-0.02	0.05	0.08	-0.06	14.5	1.7	0.48	0.93	1	0	0
3.....	HD 142	6249	4.19	0.08	0.07	0.10	0.07	0.10	0.04	10.4	6.0	0.53	0.99	0	6	0
4.....	HD 166	5577	4.58	0.12	0.10	0.08	0.11	0.18	0.11	4.1	-5.8	1.13	1.44	0	0	2
5.....	HD 283	5094	4.57	-0.47	-0.56	-0.38	-0.45	-0.55	-0.56	0.9	-42.7	0.56	1.24	1	0	0
6.....	HD 377	5873	4.28	0.11	0.00	0.05	0.07	0.15	0.04	14.6	1.5	0.70	1.04	1	0	0
7.....	HD 400	6152	4.19	-0.24	-0.30	-0.17	-0.14	-0.21	-0.29	5.7	-14.7	0.56	1.03	1	0	0
8.....	HD 531	5778	4.71	0.09	0.05	0.10	0.24	0.21	0.07	7.5	13.9	0.96	1.44	1	0	0
9.....	BD+07 9s	5707	4.62	0.03	-0.01	0.09	0.16	0.18	0.04	7.6	15.0	0.77	1.39	1	0	0
10.....	HD 691	5633	4.66	0.20	0.18	0.20	0.26	0.32	0.23	5.4	-5.3	0.66	1.72	1	0	0

NOTE.—Table 8 is available in its entirety in the electronic edition of the *Astrophysical Journal Supplement*. A portion is shown here for guidance regarding its form and content.

Generally, the R_2 plots have a better mixture of positive and negative slopes, compared to the R_1 plots, which means the pairs of associated stars provided a meaningful constraint. The R_2 plot for [M/H] suggests that [M/H] may be slightly underestimated for $T_{\text{eff}} > 6000$ K. At the warmest and coolest T_{eff} in our sample, residual abundance errors of 0.05 dex are quite possible, due in part to uncompensated errors in [M/H].

7. RESULTS

7.1. Spectroscopic Properties

Table 8 contains stellar parameters that we determined by fitting observed spectra with synthetic spectra. Column (1) contains catalog sequence numbers that run from 0 to 1040. Sequence number 0 is reserved for the Sun. Future additions to this catalog will begin at sequence number 1041. Designations for this catalog shall consist of the acronym SPOCS, which stands for Spectroscopic Parameters of Cool Stars, and a sequence number with leading zeros elided (e.g., SPOCS 42).

Column (2) lists a single name for each source, chosen in descending order of precedence from the following list of catalogs: HD, GJ (Gliese & Jahreiss 1991), BD, CD, and HIP (ESA 1997). We use current SIMBAD nomenclature to designate sources in these catalogs. We assigned a relatively low precedence to HIP catalog designations because they often do not distinguish components of binaries with separations of a few arcsec. Sources are ordered by ascending right ascension at equinox and epoch J2000 (see § 7.2). This choice of equinox and epoch facilitates automated cross-matching with other catalogs but causes HD sequence numbers to appear slightly out of sequence. Designations from all the catalogs are interleaved. In cases where we were not able to find separate coordinates for members of a close visual binary, we listed the primary first and then the secondary.

Columns (3)–(11) contain final values for the 9 global free parameters in our synthetic spectrum fitting procedure: T_{eff} , $\log g$, [M/H], [Na/H], [Si/H], [Ti/H], [Fe/H], [Ni/H], and $v \sin i$. Column (12) contains the mean radial velocity for 8 separate wavelength intervals. The corrections discussed in §§ 6.1 and 6.4 have already been applied to these stellar parameters. Table 6 gives the generic uncertainty in each parameter for a single spectrum (see § 6.3). To obtain actual uncertainties for a specific star, divide the generic uncertainties by the square-root of the number spectra that were analyzed. Table 5 contains information about the extended wings of the error distribution.

Columns (12) and (13) contain the rms residual of the synthetic spectrum fit in continuum windows and spectral line windows (see § 6.2). Columns (14)–(16) indicate the number of spectra that we analyzed from Keck, AAT, and Lick. The sum of these last three columns gives the total number of spectra, which is needed to convert generic uncertainties into actual uncertainties for a given star.

The contents of the table are available in machine-readable format from the Journal or via the VizieR catalog service.

Figure 12 shows distribution functions for stellar properties in Table 8 that we determined by fitting observations with synthetic spectra. Bin widths are half the uncertainties listed in Table 6 for a single spectrum, except for v_{rad} , which has a bin width that is 10 times the tabulated uncertainty. The distribution function for each parameter is labeled with the median value in our sample: $T_{\text{eff}} = 5755$ K, $\log g = 4.39$, [M/H] = 0.00, [Na/H] = -0.02, [Si/H] = 0.02, [Ti/H] = 0.02, [Fe/H] = 0.04, [Ni/H] = -0.01, $v \sin i = 2.4$ km s⁻¹, and $v_{\text{rad}} = 1.0$ km s⁻¹.

7.2. Derived Properties

Table 9 contains stellar properties that we either culled from the literature or derived from our spectroscopic results in Table 8. Table 9 contains the same stars as Table 8, listed in the same order. Data from the two tables may be joined into a single electronic catalog that includes columns from both tables. The data were split into two tables only to facilitate typesetting. Columns (1) and (2) in Table 9 contain catalog sequence numbers and source names from the corresponding columns in Table 8.

Columns (3) and (4) contain right ascension and declination for J2000 equinox and epoch. We adopted coordinates from the following catalogs, listed in descending order of precedence: TYC (Hog et al. 2000), HIP (ESA 1997), PPM (Roeser & Bastian 1988), and GJ (Gliese & Jahreiss 1991). The table is ordered by increasing right ascension. In a few cases we used the same coordinates for both members of a close visual binary because we were unable to find separate coordinates.

Column (5) gives apparent visual magnitude (V) taken from the following catalogs, listed in decreasing order of precedence: HIP (ESA 1997), CCDM (Dommanget & Nys 2002), and GJ (Gliese & Jahreiss 1991). We do not tabulate the uncertainty (σ_V) in V because often no estimate is provided in the source catalogs. In these cases, we adopt the V_T uncertainty in the HIP catalog, if available. Otherwise, we simply assume an uncertainty of

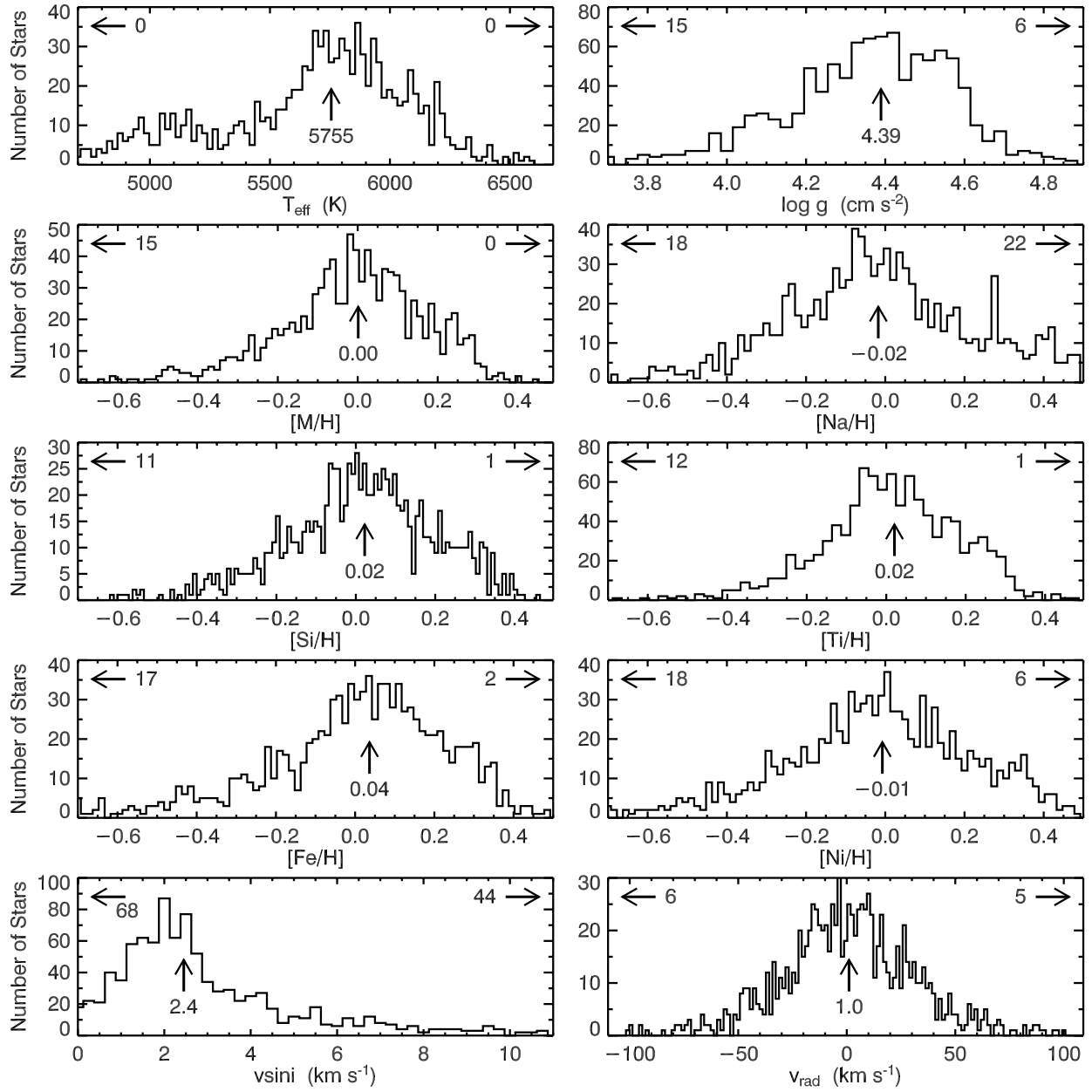


FIG. 12.—Distribution functions for stellar properties in Table 8, determined by fitting observations with synthetic spectra. Arrows pointing sideways are labeled with the number of stars at or beyond the indicated plot boundary. Arrows pointing up are located at and labeled with the median value of the stellar property being plotted.

TABLE 9
DERIVED STELLAR PARAMETERS

ID (1)	Name (2)	α (J2000) (3)	δ (J2000) (4)	V (mag) (5)	d (pc) (6)	$\log L$ (L_{\odot}) (7)	R (R_{\odot}) (8)	M (M_{\odot}) (9)	M_{iso} (M_{\odot}) (10)	ΔM_{iso} (M_{\odot}) (11)	$\log g_{\text{iso}}$ (cm s^{-2}) (12)	Age (Gyr) (13)	ΔAge (Gyr) (14)
0.....	Sun	0.000	1.000	1.000	1.01	0.99–1.03	4.44	4.3	2.6–6.0
1.....	HD 225261	00 04 56.3	+23 16 10	7.82	25.60(61)	−0.341(49)	0.811(22)	0.93(13)	0.78	0.75–0.81	4.59	8.2	0.4–14.1
2.....	HD 105	00 05 52.5	−41 45 11	7.51	40.2(1.5)	0.115(75)	1.013(39)	1.66(25)	1.17	1.12–1.21	4.33	2.8	1.0–3.5
3.....	HD 142	00 06 19.1	−49 04 30	5.80	25.64(42)	0.401(34)	1.353(24)	1.024(66)	1.24	1.22–1.26	4.32	1.9	1.0–2.6
4.....	HD 166	00 06 36.7	+29 01 17	6.07	13.70(14)	−0.215(23)	0.835(12)	0.964(93)	0.99	0.97–1.02	4.51	1.9	0.4–4.1
5.....	HD 283	00 07 32.5	−23 49 07	8.70	32.5(1.3)	−0.462(80)	0.753(32)	0.77(12)	0.71	0.68–0.74	4.67	5.5	0.1–15.0
6.....	HD 377	00 08 25.7	+06 37 00	7.59	39.8(1.5)	0.082(78)	1.060(43)	0.79(12)	1.12	1.06–1.17	4.32	4.1	1.9–5.7
7.....	HD 400	00 08 40.9	+36 37 37	6.21	33.05(75)	0.469(47)	1.510(39)	1.30(18)	1.15	1.10–1.19	4.19	4.4	3.4–5.5
8.....	HD 531	00 09 51.2	+08 27 11	9.30	70(21)	−0.10(60)	0.89(27)	1.49(91)	1.64	1.12–2.83	3.60	2.1	0.3–5.6
9.....	BD+07 9s	00 09 51.6	+08 27 11	9.30	70(21)	−0.09(60)	0.92(27)	1.27(78)	1.66	1.08–2.86	3.57	2.0	0.3–6.3
10.....	HD 691	00 11 22.4	+30 26 58	7.95	34.1(1.1)	−0.182(66)	0.851(30)	1.22(18)	1.05	1.02–1.09	4.41	4.1	1.1–6.8

NOTES.—Units of right ascension are hours, minutes, and seconds, and units of declination are degrees, arcminutes, and arcseconds. Table 9 is available in its entirety in the electronic edition of the *Astrophysical Journal Supplement*. A portion is shown here for guidance regarding its form and content.

0.01 mag, which is one unit in the least significant tabulated digit. About 95% of our sample has $0.01 \leq \sigma_V \leq 0.015$.

Column (6) gives the distance to stars in our sample ($d = 1/\pi$) and the associated uncertainty ($\sigma_d = \sigma_\pi/\pi^2$), where parallax (π) and the associated uncertainty (σ_π) came from the following catalogs, listed in decreasing order of precedence: HIP (ESA 1997), GJ (Gliese & Jahreiss 1991), and CCDM (Dommanget & Nys 2002). Parentheses after each entry enclose the uncertainty in the last two tabulated digits. For example, 25.60(61) is equivalent to 25.60 ± 0.61 and 40.2(1.5) is equivalent to 40.2 ± 1.5 . This parenthetical uncertainty notation is also used in columns (7)–(9). Most (88%) of the tabulated distances have fractional uncertainties in the range $1\% < \sigma_d/d < 10\%$ with a median of 3.0%. When $d < 2\sigma_d$ or no distance has been measured, no values are listed in columns (6)–(14).

Column (7) contains logarithmic luminosity ($\log L$) in solar units and the associated uncertainty ($\sigma_{\log L}$), which we calculated using the formulae

$$\log L = -0.4(V + 5 \log \pi + 5 + \Delta V - M_{\text{bol},\odot}), \quad (3)$$

$$\sigma_{\log L} = 0.921 \sqrt{\sigma_V^2 + \left(\frac{2.171 \sigma_\pi}{\pi}\right)^2}, \quad (4)$$

where ΔV converts absolute magnitude in the V band to bolometric magnitude and $M_{\text{bol},\odot}$ is the bolometric magnitude of the Sun. These formulae neglect interstellar extinction and errors in ΔV . We obtained a bolometric correction, ΔV , for each star by interpolating in the “high-temperature” grid of Vandenberg & Clem (2003), using our spectroscopically determined T_{eff} , $\log g$, and $[M/H]$ from Table 8. This procedure yielded $\Delta V = -0.094$ and $M_{\text{bol},\odot} = 4.727$ for the Sun, assuming $V = -26.75$ and a mean distance of 1 AU (Cox 2000). Uncertainties are expressed using parenthetical notation, as in column (6). Most (90%) of the tabulated luminosities have fractional uncertainties in the range $2\% < \sigma_L/L < 20\%$ with a median of 6.2%.

Column (8) contains stellar radius (R) in solar units and the associated uncertainty (σ_R), which we calculated using the formulae

$$\frac{R}{R_\odot} = \sqrt{\frac{L}{L_\odot} \left(\frac{T_\odot}{T_{\text{eff}}}\right)^2}, \quad (5)$$

$$\sigma_R = R \sqrt{\left(\frac{\sigma_L}{L}\right)^2 + \left(\frac{2\sigma_T}{T_{\text{eff}}}\right)^2}, \quad (6)$$

where $T_\odot = 5770$ K is the effective temperature of the Sun. We used our spectroscopically determined T_{eff} from Table 8 and computed σ_T using data from Tables 6 and 8 (see § 6.3). Uncertainties in our computed radii are dominated by uncertainties in distance and hence luminosity, rather than errors in T_{eff} . Uncertainties are expressed using parenthetical notation, as in column (6). Most (94%) of the tabulated radii have fractional uncertainties in the range $1\% < \sigma_R/R < 10\%$ with a median of 3.3%.

Column (9) contains stellar mass (M) in solar units and the associated uncertainty (σ_M), which we calculated using the formulae

$$\frac{M}{M_\odot} = \left(\frac{R}{R_\odot}\right)^2 10^{\log g - \log g_\odot}, \quad (7)$$

$$\sigma_M = M \sqrt{\left(\frac{\sigma_{\log g}}{\log e}\right)^2 + \left(\frac{2\sigma_R}{R}\right)^2}, \quad (8)$$

where $\log g_\odot = 4.437 \text{ cm s}^{-2}$ is the surface gravity of the Sun. We used our spectroscopically determined $\log g$ from Table 8 and computed $\sigma_{\log g}$ using data from Tables 6 and 8 (see § 6.3). Uncertainties in our computed masses are dominated by uncertainties in $\log g$, rather than errors in radius. Uncertainties are expressed using parenthetical notation, as in column (6). Many (69%) of the tabulated masses have fractional uncertainties in the range $10\% < \sigma_M/M < 20\%$ with a median of 14.3%.

Columns (10)–(14) of Table 9 give quantities determined by interpolating in a grid of isochrones, as described in § 8.

Figure 13 shows distribution functions for stellar properties in Table 9, which we culled from the literature, derived from our spectroscopic properties in Table 8, or obtained by interpolating isochrones (see § 8). We used bin widths of 0.15 mag for V , 2.5 pc for d , 0.05 for $\log L/L_\odot$, R/R_\odot , and M/M_\odot , and 0.5 Gyr for age. The distribution function for each parameter is labeled with the median value in our sample: $V = 7.15$ mag, $d = 33.2$ pc, $\log L = 0.13 \log L_\odot$, $R = 1.12 R_\odot$, $M = 1.14 M_\odot$, $M_{\text{iso}} = 1.06 M_\odot$, and an age of 4.5 Gyr.

7.3. HR Diagram

Figure 14 is a Hertzsprung-Russell (HR) diagram, showing $\log L$ based on observed brightness and measured distance (Table 9) versus T_{eff} determined in our spectroscopic analysis (Table 8). Curves show theoretical isochrones for stellar populations with the solar iron abundance and ages of 0.1, 5, and 10 Gyr. We use Yonsei-Yale (Y^2) isochrones (Demarque et al. 2004) to interpret our results because Hillenbrand & White (2004) conclude that Y^2 isochrones offer the best overall agreement with dynamical masses for main-sequence stars down to $0.4 M_\odot$.

The locus of observed points in the HR diagram is generally consistent with theoretical isochrones for $[\text{Fe}/H] = 0$, which is equivalent to the median $[\text{Fe}/H]$ in our sample of 0.04. Stars warmer than 5600 K fill the region between the 0.1 and 10 Gyr isochrones, indicating a large spread in stellar ages. Stars cooler than 5600 K form a narrow main-sequence, implying a relatively small spread in $[\text{Fe}/H]$, which is consistent with the distribution function we derived spectroscopically (see Fig. 12). Outliers below the main-sequence tend to be metal-poor, while those above tend to be metal-rich, though there are exceptions. Isochrones predict this general behavior, as we discuss next.

Figure 15 shows how the isochrones respond to changes of ± 0.5 in $[\text{Fe}/H]$ and $+0.3$ in $[\alpha/\text{Fe}]$. The parameter $[\text{Fe}/H]$ refers specifically to iron abundance, not general metallicity. The parameter $[\alpha/\text{Fe}]$ is the logarithmic abundance of certain elements formed by α -capture in the nucleus (e.g., Si, Mg, and Ti), relative to the abundance of iron, all referenced to solar values for the same quantities. By definition, $[\alpha/\text{Fe}] = 0$ for the Sun. Kim et al. (2002) tabulate the pattern of abundance changes in Y^2 models with nonsolar values of $[\alpha/\text{Fe}]$. For our subset of elements with measured abundances, they assumed that $[\text{Na}/\text{Fe}] = [\text{Si}/\text{Fe}] = [\text{Ti}/\text{Fe}] = [\alpha/\text{Fe}]$ and $[\text{Ni}/\text{Fe}] = 0$. We measured $[\text{Si}/H]$ more precisely than $[\text{Na}/H]$ or $[\text{Ti}/H]$ (see Table 6), so we adopt $[\text{Si}/\text{Fe}] = [\text{Si}/H] - [\text{Fe}/H]$ as an observational proxy for $[\alpha/\text{Fe}]$, when interpolating Y^2 isochrones. Our measured values of $[\text{Si}/\text{Fe}]$ range between -0.31 and $+0.66$ with a median of 0.00.

7.4. Surface Gravity

Figure 16 compares our spectroscopic measurements of $\log g$ and T_{eff} from Table 8 with theoretical isochrones. Our purely spectroscopic measurements imply younger ages than the parallax-based HR diagram (Fig. 14). Since both diagrams have the

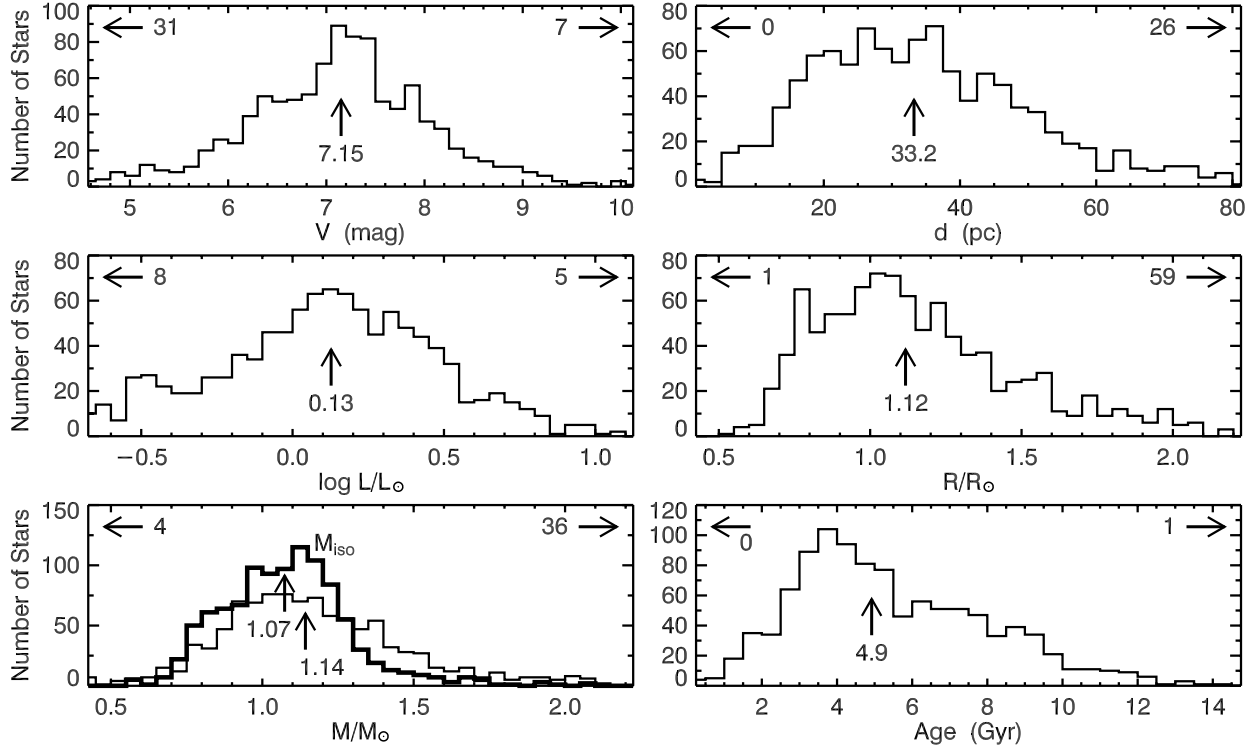


FIG. 13.—Distribution functions for stellar properties in Table 9, derived from the literature (V , d , and $\log L/\log L_\odot$), measured spectroscopically, or determined by interpolating isochrones (M/M_\odot). Arrows pointing sideways are labeled with the number of stars beyond the indicated plot boundary. Arrows pointing up are located at and labeled with the median value of the stellar property being plotted. Separate distribution functions are shown for masses derived from our spectroscopic gravities (*thin histogram*) or from interpolating isochrones (*thick histogram*).

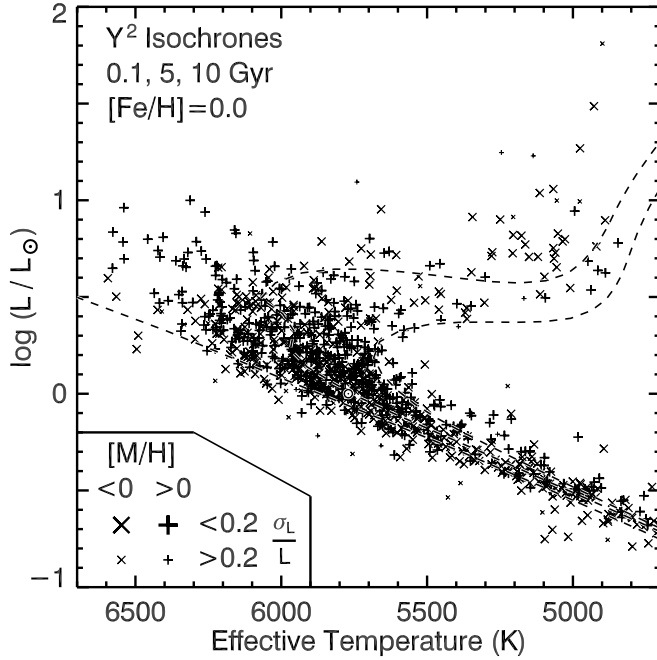


FIG. 14.—This HR diagram shows measured $\log L$ (Table 9) vs. spectroscopic T_{eff} (Table 8). Symbol type distinguishes between low-metallicity (*crosses*) and high-metallicity (*pluses*) stars. Stars with relatively imprecise $\log L$ are plotted with smaller symbols. Isochrones show the predicted loci of $[\text{Fe}/\text{H}] = 0$ stars at ages of 0.1, 5, and 10 Gyr. The Sun is represented by a circle at $T_{\text{eff}} = 5700$ K. [See the electronic edition of the *Journal* for a color version of this figure.]

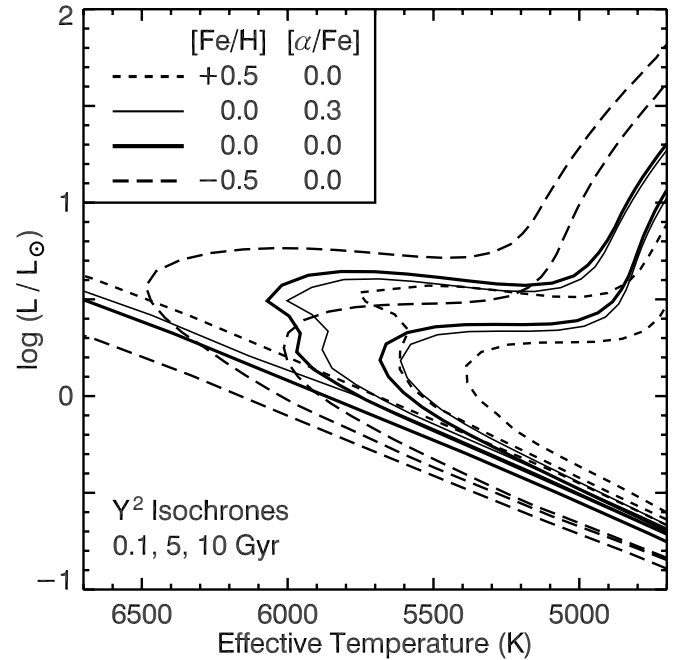


FIG. 15.—Overlay for Fig. 14 showing how Y^2 isochrones change for non-solar values of $[\text{Fe}/\text{H}]$ and $[\alpha/\text{Fe}]$. $[\alpha/\text{Fe}]$ is the logarithmic abundance (relative to iron) of elements formed by α -capture, such as Si, Mg, and Ti. [See the electronic edition of the *Journal* for a color version of this figure.]

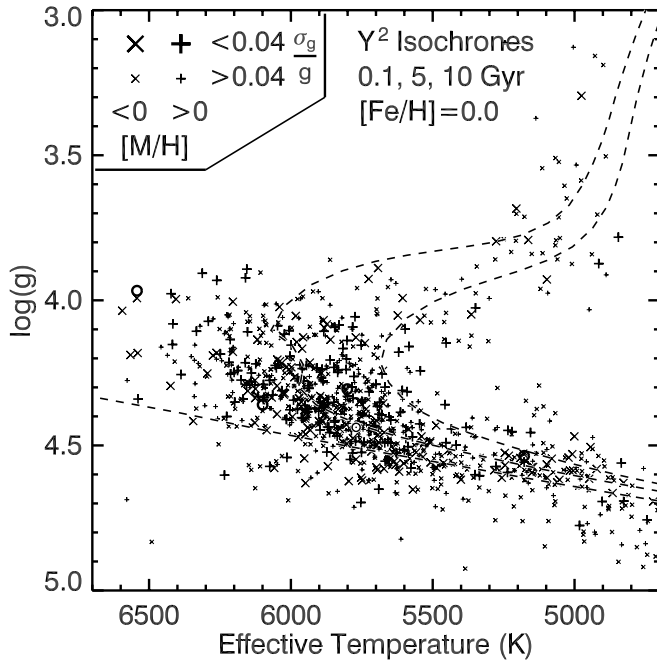


FIG. 16.—Plot of $\log g$ vs. T_{eff} with Y^2 isochrones for $[\text{Fe}/\text{H}] = 0$. The Sun is represented by a circle at $T_{\text{eff}} = 5770$ K. Four stars with accurate based on measured angular diameters and dynamical masses are indicated with circles. [See the electronic edition of the Journal for a color version of this figure.]

same T_{eff} axis, the discrepancy is presumably in $\log g$. Our spectroscopic $\log g$ values seem to be shifted downward (toward higher gravity) by roughly 0.1 dex, relative to the isochrones. Models of stellar interiors and atmospheres are both sufficiently complex that either might be the source of the discrepancy. Figure 17 shows how the isochrones respond to changes in $[\text{Fe}/\text{H}]$ and $[\alpha/\text{Fe}]$.

Spectroscopic gravity determinations can be biased by correlated errors in T_{eff} or elemental abundances. In particular, we used the Mg I b triplet to constrain $\log g$, but our wavelength intervals contained no other atomic lines that could be used to constrain Mg abundance. We assumed that $[\text{Mg}/\text{Fe}] = 0$, when in fact $[\text{Mg}/\text{Fe}]$ generally increases with decreasing $[\text{Fe}/\text{H}]$ (e.g., Mashonkina et al. 2003), giving rise to potential errors in $\log g$ at low metallicity.

In addition, the fidelity of our analysis is limited by the various empirical corrections that we applied (see §§ 3.3, 6.1, and 6.4). For example, we decreased our raw gravities (shifted them up in Fig. 16) by 0.074 dex (see Table 4) to force our analysis of the solar spectrum (Vesta) to yield the solar gravity. Measurements of dynamical mass and angular diameter provide an alternate way to measure gravities (see the end of § 8), but unfortunately only a few stars have accurate measurements.

Table 10 compares our spectroscopic gravities for Procyon A, α Cen A, and α Cen B with accurate measurements based on dynamical masses, measured angular diameters, and accurate parallaxes. HD 209458 has a transiting planet, so only the radius is known accurately. Our spectroscopic gravities agree well with these four direct measurements.

7.5. Literature Comparisons

A number of fine spectral analyses have been carried out on nearby stars and overlap with subsets of the sample analyzed here. Comparing the results from this catalog with electronically available results for some of the larger high-precision spectro-

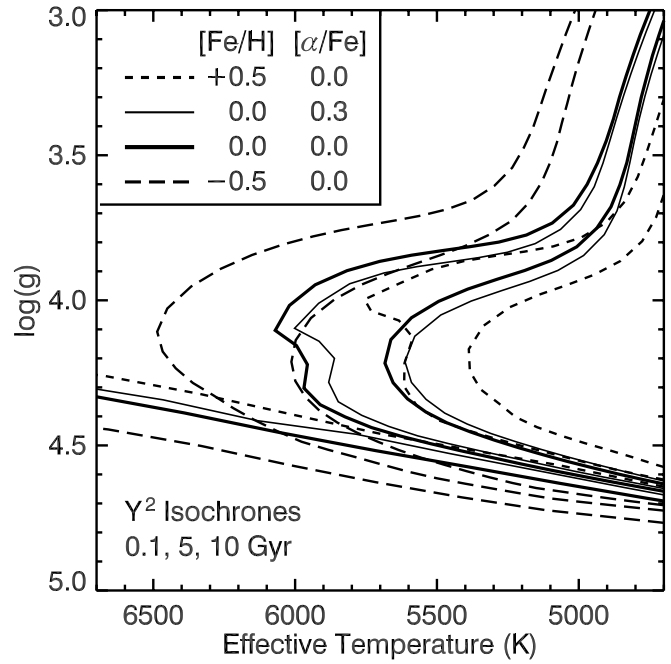


FIG. 17.—Plot of $\log g$ vs. T_{eff} with Y^2 isochrones, again showing locus shifts for nonsolar patterns in α -elements. [See the electronic edition of the Journal for a color version of this figure.]

scopic programs, we find good agreement for T_{eff} (Fig. 18) and $[\text{Fe}/\text{H}]$ (Fig. 19). There is more scatter in the comparison for $\log g$ (Fig. 20), consistent with larger fractional errors for this parameter. Table 11 gives the mean rms differences between the SPOCS catalog and corresponding literature values.

8. ISOCHRONE ANALYSIS

8.1. Methodology

Thus far, we have considered stellar properties that were determined spectroscopically (see Table 8), measured directly (V and d), or calculated from some combination ($\log L$, R , and M). Using these results, we constructed an HR diagram for our sample (§ 7.3). In this section, we interpret our observed HR diagram, using of Y^2 isochrones (version 2) from theoretical stellar evolution models (Demarque et al. 2004). This analysis yields theoretical estimates of mass (M_{iso}), radius (R_{iso}), and surface gravity ($\log g_{\text{iso}}$), as well as age constraints. The procedure is complicated because the isochrones are multidimensional, non-uniformly spaced, and nonmonotonic.

The Y^2 isochrones tabulate T_{eff} , $\log L$, $\log g_{\text{iso}}$, M_V , and numerous colors (Lejune et al. 1998), as a function of $[\text{Fe}/\text{H}]$, $[\alpha/\text{Fe}]$, age, and M_{iso} . Four measured quantities are needed to isolate a particular stellar state. In our isochrone analysis, we specified states, using our spectroscopically determined T_{eff} , $[\text{Fe}/\text{H}]$, and $[\alpha/\text{Fe}]$, together with $\log L$, which also depends on our spectroscopic analysis via the bolometric correction. We interpolated the tables to the desired value of $[\alpha/\text{Fe}]$ and then interpolated again to the desired value of $[\text{Fe}/\text{H}]$, yielding one set of tabulated isochrones for ages between 0.01 and 15 Gyr. We then interpolated each isochrone to the desired value of T_{eff} , obtaining zero, one, or multiple solutions for each isochrone, depending on the shape and location of each isochrone on the HR diagram. Finally, we interpolated each possible solution ($\log L$ as a function of age) to the desired value of $\log L$, obtaining a single stellar state for each possible solution.

TABLE 10
COMPARISON WITH INDEPENDENTLY MEASURED STELLAR GRAVITIES

ID	NAME	LITERATURE MASS		LITERATURE RADIUS		Lit. $\log g$ (cm s^{-2})	Spec. $\log g$ (cm s^{-2})	Iso. $\log g$ (cm s^{-2})
		(M_{\odot})	Reference	(R_{\odot})	Reference			
354.....	HD 61421	1.42(06)	1	2.048(25)	2	3.967(49)	3.993(29)	4.05
612.....	HD 128621	0.9340(61)	3	0.863(05)	4	4.536(13)	4.558(25)	4.50
613.....	HD 128620	1.1050(70)	3	1.224(03)	4	4.306(08)	4.331(29)	4.31
960.....	HD 209458	1.10(10)	5	1.146(50)	6	4.36(13)	4.382(50)	4.39

NOTE.—Parentheses enclose the 1σ uncertainty in the last two tabulated digits of each measured or calculated value.

REFERENCES.—(1) Allende Prieto et al. 2002; (2) Kervella et al. 2004; (3) Pourbaix et al. 2002; (4) Kervella et al. 2003; (5) Mazeh et al. 2000; (6) Brown et al. 2001.

To assess how uncertainties in our four measured quantities propagate into stellar properties derived from the isochrones, we repeated the isochrone analysis with perturbed values of T_{eff} , $[\text{Fe}/\text{H}]$, $[\alpha/\text{Fe}]$, and $\log L$. We varied each parameter from -4σ below the nominal value (x_0) to $+4\sigma$ above nominal in 17 steps of 0.5σ , for a total of 83,521 parameter combinations per star. Each specific parameter value,

$$x_k = x_0 + \frac{k\sigma}{2}, \quad (9)$$

represents a range of possible values between $x_0 + (k - 0.5)\sigma/2$ and $x_0 + (k + 0.5)\sigma/2$ for our bin width of 0.5σ . We assumed that errors in the input parameters are normally distributed, so

the probability (p_k) of realizing a parameter value in a particular bin is

$$p_k = \frac{1}{2} \left[\text{erf} \left(\frac{k + 0.5}{2\sqrt{2}} \right) - \text{erf} \left(\frac{k - 0.5}{2\sqrt{2}} \right) \right]. \quad (10)$$

For perturbations of zero to $+4\sigma$ (integer values of k from 0 to 8), p_k has the values 0.197, 0.175, 0.121, 0.0656, 0.0278, 0.00924, 0.00240, 0.000489, and 0.0000777.

Considering only measurement error and ignoring covariances, the probability of realizing any particular quartet of input parameters is simply the product of the probabilities of each individual parameter value. However, the probability of a star being in a particular stellar state also depends on the time (τ) stars

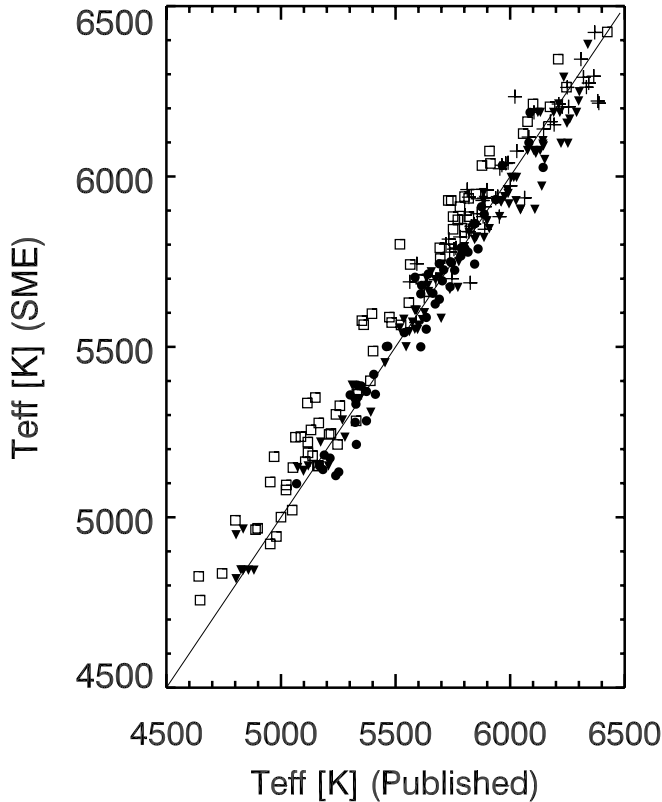


FIG. 18.—Comparison of T_{eff} from this catalog with Allende Prieto et al. (2004) (squares), Edvardsson et al. (1993) (pluses), Santos et al. (2004) (downward triangles), and Fuhrmann et al. (1997, 1998) (filled circles). [See the electronic edition of the Journal for a color version of this figure.]

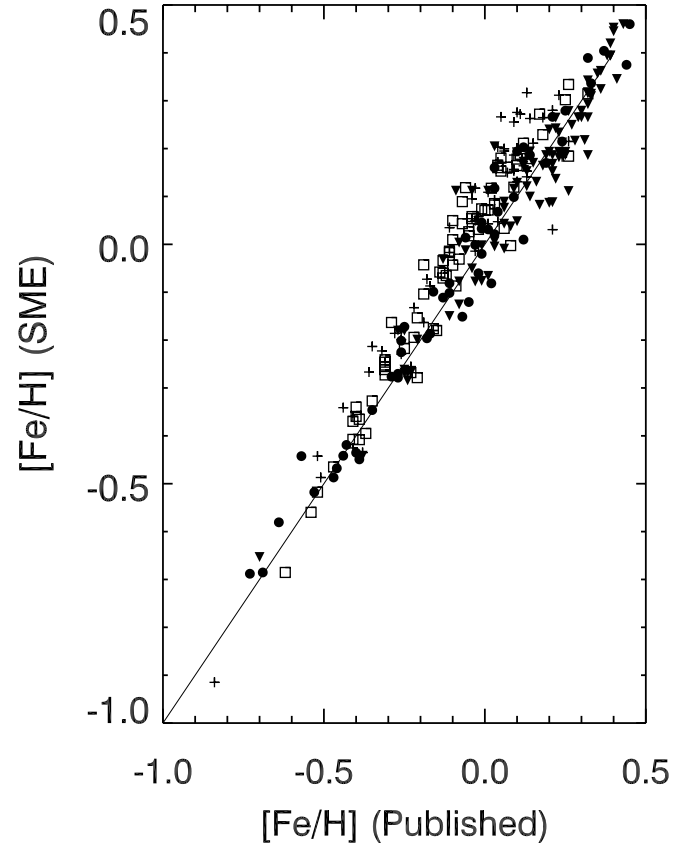


FIG. 19.—Same as Fig. 18, except for $[\text{Fe}/\text{H}]$. Small systematic shifts distinguish the different analyses. [See the electronic edition of the Journal for a color version of this figure.]

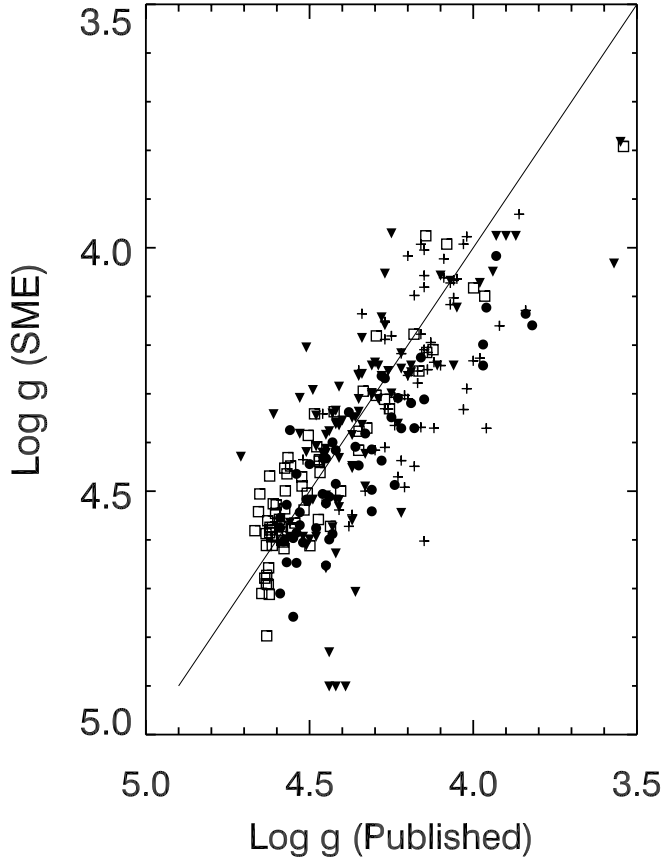


FIG. 20.—Same as Fig. 18, except for $\log g$. Typical errors in $\log g$ are ~ 0.1 dex. Four stars with accurate gravities based on measured angular diameters and dynamical masses are also shown (open circles). [See the electronic edition of the Journal for a color version of this figure.]

remain in that state. We estimated the minimum and maximum stellar age in a particular isochrone bin by interpolating age as a function of $\log L$ in the final interpolation step, using the minimum and maximum $\log L$ for the bin. The difference of these two ages yielded τ , which we use to weight the measurement probability, obtaining the unnormalized probability (U) of observing a particular state,

$$U = P T_{\text{eff}} P_{[\text{Fe}/\text{H}]} P_{[\alpha/\text{Fe}]} P_{\log L \tau}. \quad (11)$$

Normalizing the 83,521 values of u for a particular star yields the probability (P) of each state in our uncertainty analysis. We followed the error distributions out to 4σ because τ can vary by orders of magnitude for plausible changes in input parameters. Our analysis technique could be further improved by considering the volume of space probed by our magnitude-limited sample (favors brighter stars) and the initial mass function (favors low-mass stars).

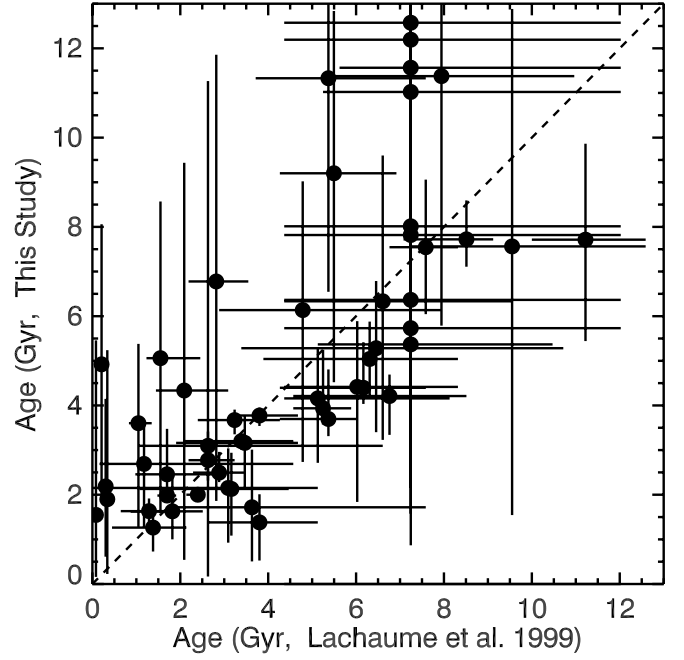


FIG. 21.—Comparison of ages and corresponding uncertainties determined in this study with results from Lachaume et al. (1999) for a small subset of stars in common. Results from the two studies are generally consistent.

Finally, to determine the median and 1σ limits for M_{iso} , R_{iso} , $\log g_{\text{iso}}$, and age, we sorted into ascending order all 83,521 possible values for each of these derived properties. We then constructed a cumulative probability distribution function (C) for the equivalently sorted probabilities, P . We adopted the value where $C = 0.5$ as the best estimate of the derived property. For 1σ limits, we adopted the values where $C = 0.157$ and 0.843 . In a significant number of cases, the 1σ limits span almost the entire main-sequence lifetime of the star. Our isochrone analysis provides no significant age constraint in these cases. Figure 21 compares our ages and 1σ uncertainties with the results of a similar type of analysis by Lachaume et al. (1999). Our 1σ limits on age are slightly larger because we extended the error distributions for our input parameters from $\pm 3\sigma$ to $\pm 4\sigma$.

8.2. Results

Columns (10)–(14) of Table 9 contain the results of our isochrone interpolation analysis. Column (10) gives the most likely mass (M_{iso}). Column (11) bounds the 1σ range of masses allowed by 1σ changes only in $\log L$. Column (12) gives the most likely surface gravity ($\log g_{\text{iso}}$). Radius (R_{iso}) can be computed from these two columns. Column (13) gives an age estimate. Column (14) bounds the 1σ range of ages allowed by 1σ changes only in $\log L$. The ages must be considered preliminary at this point, as they have not yet been critically examined. Chromospheric

TABLE 11
COMPARISON WITH PUBLISHED VALUES

Reference	T_{eff} rms (K)	$[\text{Fe}/\text{H}]$ rms	$\log g$ rms (cm s^{-1})	Number of Stars
Edvardsson et al. (1993).....	93	0.07	0.15	62
Fuhrmann et al. (1997, 1998).....	58	0.05	0.10	52
Santos et al. (2004).....	63	0.06	0.16	92
Allende Prieto et al. (2004).....	77	0.06	0.08	71

activity measurements would provide a weak additional constraint on stellar age.

The bottom two panels of Figure 13 show the distributions of M_{iso} and ages from the isochrone interpolation analysis. The mass plot also shows the distribution of M that we derived from our spectroscopic $\log g$. Our spectroscopic masses are systematically larger than masses based on evolutionary models and accurate parallaxes. The median ratio of the two mass estimates is 1.09, corresponding to a systematic error of 0.04 dex in $\log g$. For 20 stars in the sample, the mass ratio exceeds a factor of 2, implying errors in $\log g$ greater than 0.3 dex. Above this threshold, spectroscopic gravities and coupled parameters (e.g., T_{eff}) probably have errors that significantly exceed the generic uncertainties in Table 6.

Accurate dynamical masses from binary orbits could be used to investigate the discrepancy, except that accurate measurements exist for only four stars in our sample. The fractional error in $\log g$ is approximately half the fractional error in M , so it is advantageous to compare gravities rather than masses, as in Table 10. Unfortunately, accurate dynamical masses are not available for any of the stars with a large mass discrepancy in Table 9.

9. CONCLUSIONS

We analyzed uniformly spectra of 1040 F, G, and K stars in the Keck, Lick, and AAT planet search programs, deriving stellar parameters (T_{eff} , $\log g$, $v \sin i$, $[M/H]$, and individual elemental abundances for Fe, Ni, Si, Na, and Ti) with a precision per spectrum of 44 K for T_{eff} , 0.06 dex for $\log g$, 0.5 km s⁻¹ for $v \sin i$, and 0.03 dex for $[M/H]$. We then used the spectroscopic results to select appropriate isochrones for each star, deriving theoretical masses, gravities, radii, and age constraints. We find that our spectroscopic gravities systematically exceed gravities from isochrones by about 0.1 dex, with corresponding biases in spectroscopically derived masses and radii. Our results for all stars are tabulated in the electronic edition of this Journal and in the VizieR catalog service.²

From an analysis standpoint, our purely spectroscopic technique appears to be unique, at least for large surveys of cool stars. Additional brightness and color constraints can improve accuracy for stars with accurate parallaxes, but our purely spectroscopic approach works equally well for more distant stars. From a practical standpoint, the large size of our uniformly analyzed sample also appears to be unique, enabling studies that have not been possible with smaller samples. For example, we determined new relationships between $B - V$ and T_{eff} and between v_{mac} and

T_{eff} . We also explored the limitations of commonly used spectrum synthesis tools, noting a small systematic discrepancy between gravities determined spectroscopically and by interpolating theoretical isochrones. Selection effects in our sample must be considered before using our results to study chemical evolution in the Galaxy.

The internal consistency of this analysis of all stars in a large planet search program makes it ideal for investigating the correlation between stellar metallicity and the presence of gas giant planets (Fischer & Valenti 2005) or for developing photometric indexes that predict T_{eff} , $\log g$, and $[Fe/H]$. Our results should also serve the needs of space missions, such as the *Spitzer Space Telescope*, the *Space Interferometry Mission*, the *James Webb Space Telescope*, and the *Terrestrial Planet Finder*, providing fundamental information on some of the most desirable candidate target stars with a heritage of Doppler information.

This work is the first installment in the SPOCS (Spectroscopic Properties of Cool Stars) Catalog. The next installment will be based on spectra obtained by the N2K program (Fischer et al. 2005), a high-precision radial velocity survey of the “Next 2000” brightest stars that are not currently being monitored. We invite other groups with echelle spectra of many cool stars to contact us about the possibility of collaborating on additional contributions to the SPOCS Catalog.

We are indebted to Geoff Marcy for ongoing useful conversations and to the many colleagues who collected template spectra for the Doppler planet search projects over the past decade, including Paul Butler, Geoff Marcy, Steve Vogt, Chris McCarthy, Jason Wright, John Johnson, Chris Tinney, Hugh Jones, Alan Penny, and Brad Carter. We also thank our many colleagues who allowed us to use their computers for this project. We gratefully acknowledge the dedication of the staff at the Keck, Anglo-Australian and Lick Observatories. We thank the University of California and NASA time allocation committees for telescope time at Lick and Keck Observatories. We acknowledge salary support for Fischer by NASA through grant NAG5-75005 (to Geoff Marcy) and thank Sun Microsystems. This research has made use of the SIMBAD database, operated at CDS, Strasbourg, France and the Vienna Atomic Line Database, and the Kurucz Atomic and Molecular line Databases, and the NIST Atomic Spectra Database. The authors extend special thanks those of Hawai’ian ancestry on whose sacred mountain of Mauna Kea we are privileged to be guests. Without their generous hospitality, the Keck observations presented here would not have been possible.

² See <http://vizier.u-strasbg.fr/>.

REFERENCES

- Allende Prieto, C., Asplund, M., García López, R. J., & Lambert, D. L. 2002, *ApJ*, 573, L137
 Allende Prieto, C., Barklem, P. S., Lambert, D. L., & Cunha, K. 2004, *A&A*, 420, 183
 Anders, E., & Grevesse, N. 1989, *Geochim. Cosmochim. Acta*, 53, 197
 Asplund, M., Nordlund, Å., Trampedach, R., Allende Prieto, C., & Stein, R. F. 2000, *A&A*, 359, 729
 Balachandran, S. 1990, *ApJ*, 354, 310
 Barklem, P. S., Piskunov, N., & O’Mara, B. J. 2000, *A&AS*, 142, 467
 Brown, T. M., Charbonneau, D., Gilliland, R. L., Noyes, R. W., & Burrows, A. 2001, *ApJ*, 552, 699
 Butler, R. P., Marcy, G. W., Vogt, S. S., Fischer, D. A., Henry, G. W., Laughlin, G., & Wright, J. T. 2003, *ApJ*, 582, 455
 Butler, R. P., Marcy, G. W., Williams, E., McCarthy, C., Dosanji, P., & Vogt, S. S. 1996, *PASP*, 108, 500
 Cayrel de Strobel, G., Soubiran, C., & Ralite, N. 2001, *A&A*, 373, 159
 Cox, A. N., ed. 2000, *Allen’s Astrophysical Quantities* (4th ed.; New York: AIP)
 Cummings, A., Marcy, G. W., & Butler, R. P. 1999, *ApJ*, 526, 890
 de Bièvre, P., & Barnes, I. L. 1985, *Int. J. Mass Spectrom. Ion Processes*, 65, 211
 Demarque, P., Woo, J.-H., Kim, Y.-C., & Yi, S. K. 2004, *ApJS*, 155, 667
 Diego, F., Charalambous, A., Fish, A. C., & Walker, D. D. 1990, *Proc. SPIE*, 1235, 562
 Dommanget, J., & Nys, O. 2002, *Obs. et Travaux*, 54, 5
 Edvardsson, B., Andersen, J., Gustafsson, B., Lambert, D. L., Nissen, P. E., & Tomkin, J. 1993, *A&A*, 275, 101
 Erspamer, D., & North, P. 2002, *A&A*, 383, 227
 ESA. 1997, *The Hipparcos and Tycho Catalogues* (ESA SP-1200; Noordwijk: ESA)
 Fischer, D. A., Marcy, G. W., Butler, R. P., Vogt, S. S., & Apps, K. 1999, 111, 50
 Fischer, D. A., & Valenti, J. A. 2005, *ApJ*, 622, 1102
 Fischer, D. A., et al. 2005, *ApJ*, 620, 481
 Fuhrmann, K., Pfeiffer, M. J., & Bernkopf, J. 1997, *A&A*, 326, 1081
 ———. 1998, *A&A*, 336, 942

- Gliese, W., & Jahreiss, H. 1991, Preliminary Version of the Third Catalogue of Nearby Stars (Heidelberg: Astron. Rechen-Institut)
- Gray, D. F. 1988, Lectures on Spectral Line Analysis: F, G, and K Stars (Ontario: Aylmer)
- Hillenbrand, L. A., & White, R. J. 2004, *ApJ*, 604, 741
- Hinkle, K., Wallace, L., Valenti, J. A., & Harmer, D., eds. 2000, in Visible and Near Infrared Atlas of the Arcturus Spectrum 3727–9300 Å (San Francisco: ASP)
- Hog, E., et al. 2000, *A&A*, 355, L27
- Holweger, H., Bard, A., Kock, M., & Kock, A. 1991, *A&A*, 249, 545
- Kervella, P., Thévenin, F., Morel, P., Berthomieu, G., Bordé, P., & Provost, J. 2004, *A&A*, 413, 251
- Kervella, P., Thévenin, F., Ségransan, D., Berthomieu, G., Lopez, B., Morel, P., & Provost, J. 2003, *A&A*, 404, 1087
- Kim, Y.-C., Demarque, P., Yi, S. K., & Alexander, D. R. 2002, *ApJS*, 143, 499
- Kupka, F., Piskunov, N. E., Ryabchikova, T. A., Stempels, H. C., & Weiss, W. W. 1999, *A&AS*, 138, 119
- Kurucz, R. L. 1992, in IAU Symp. 149, The Stellar Populations of Galaxies, ed. B. Barbuy & A. Renzini (Dordrecht: Reidel), 225
- . 1993a, ATLAS9 Stellar Atmosphere Programs and 2 km/s Grid (Kurucz CD-ROM 13) (Cambridge: SAO)
- . 1993b, SYNTHE Spectrum Synthesis Programs and Line Data (Kurucz CD-ROM 18) (Cambridge: SAO)
- . 1994a, Atomic Data for Ca, Sc, Ti, V, and Cr (Kurucz CD-ROM 20) (Cambridge: SAO)
- . 1994b, Atomic Data for Mn and Co (Kurucz CD-ROM 21) (Cambridge: SAO)
- . 1994c, Atomic Data for Fe and Ni (Kurucz CD-ROM 22) (Cambridge: SAO)
- Kurucz, R. L., Furenlid, I., Brault, J., & Testerman, L. 1984, National Solar Observatory Atlas No. 1: Solar Flux Atlas from 296 to 1300 nm (Sunspot: National Solar Observatory)
- Lachaume, R., Dominik, C., Lanz, T., & Habing, H. J. 1999, *A&A*, 348, 897
- Lejune, Th., Cuisinier, F., & Buser, R. 1998, *A&AS*, 130, 65
- Marcy, G. W., Butler, R. P., Fischer, D. A., & Vogt, S. S. 2004, in ASP Conf. Ser. 321, Extrasolar Planets: Today and Tomorrow, ed. J.-P. Beaulieu, A. Lecavalier des Etangs, & C. Terquem (San Francisco: ASP), 3
- Marcy, G. W., Butler, R. P., Vogt, S. S., Fischer, D. A., Henry, G. W., Wright, J. T., & Johnson, J. A. 2005, *ApJ*, 619, 570
- Mashonkina, L., Gehren, T., Travaglio, C., & Borkova, T. 2003, *A&A*, 397, 275
- Mazeh, T., et al. 2000, *ApJ*, 532, L55
- McWilliam, A. 1990, *ApJS*, 74, 1075
- Mihalas, D. 1978, *Stellar Atmospheres* (San Francisco: Freeman)
- Moultaka, J., Ilovaisky, S. A., Prugniel, P., & Soubiran, C. 2004, *PASP*, 116, 693
- Mulas, G., Modigliani, A., Porceddu, I., & Damiani, F. 2002, *Proc. SPIE*, 4844, 310
- Nichols, J. S., & Linsky, J. L. 1996, *AJ*, 111, 517
- Nidever, D. L., Marcy, G. W., Butler, R. P., Fischer, D. A., & Vogt, S. S. 2002, *ApJS*, 141, 503
- Noyes, R. W., Hartmann, L. W., Baliunas, S. L., Duncan, D. K., & Vaughan, A. H. 1984, *ApJ*, 279, 763
- Perrier, C., Sivan, J.-P., Naef, D., Beuzit, J. L., Mayor, M., Queloz, D., & Udry, S. 2003, *A&A*, 410, 1039
- Piskunov, N. E., Kupka, F., Ryabchikova, T. A., Weiss, W. W., & Jeffery, C. S. 1995, *A&AS*, 112, 525
- Piskunov, N. E., & Valenti, J. A. 2002, *A&A*, 385, 1095
- Pourbaix, D., et al. 2002, *A&A*, 386, 280
- Roeser, S., & Bastian, U. 1988, *A&AS*, 74, 449
- Saar, S. H., & Osten, R. A. 1997, *MNRAS*, 284, 803
- Santos, N. C., Israelian, G., & Mayor, M. 2004, *A&A*, 415, 1153
- Unsöld, A. 1955, *Physik der Sternatmosphären* (Berlin: Springer)
- Valenti, J. A. 1994, Ph.D. thesis, Univ. California, Berkeley
- Valenti, J. A., Butler, R. P., & Marcy, G. W. 1995, *PASP*, 107, 966
- Valenti, J. A., & Piskunov, N. E. 1996, *A&AS*, 118, 595
- Valenti, J. A., Piskunov, N. E., & Johns-Krull, C. M. 1998, *ApJ*, 498, 851
- VandenBerg, D. A., & Clem, J. L. 2003, *AJ*, 126, 778
- Vogt, S. S. 1987, *PASP*, 99, 1214
- Vogt, S. S., et al. 1994, *Proc. SPIE*, 2198, 362
- Wallace, L., Hinkle, K., & Livingston, W. 1998, An Atlas of the Spectrum of the Solar Photosphere from 13,500 to 28,000 cm⁻¹ (3570 to 7405 Å) (Tucson: NOAO)